



POLITECNICO
MILANO 1863

SCUOLA DI INGEGNERIA INDUSTRIALE
E DELL'INFORMAZIONE

Optimization of YBCO nanostructures for SQUID applications

TESI DI LAUREA MAGISTRALE IN
PHYSICS ENGINEERING - INGEGNERIA FISICA

Author: **Alessia Garibaldi**

Student ID: 928599

Advisor: Prof. Giacomo Claudio Ghiringhelli

Co-advisors: Dr Edoardo Trabaldo, Prof. Thilo Bauch

Academic Year: 2021-22

Abstract

This thesis work focuses on the optimization of High Temperature Superconductor (HTS) $\text{YBa}_2\text{Cu}_3\text{O}_{7-\delta}$ (YBCO) nanoscaled devices, specifically Groove Dayem nanoBridges (GDB), for Superconducting QUantum Interferences Devices (SQUID) applications. YBCO-based weak links are a major focus of research in the field of superconducting sensors, such as ultra-sensitive magnetometers, due to the valuable improvements that using HTS materials would add, with higher working temperatures and critical magnetic fields, to the research and to the commercial aspect of these technologies. In this work, we aim specifically to fabricate and improve GDB-based SQUIDs, which were shown to have promising performances at the HTS working temperature, $T = 77$ K, although not yet comparable to the state-of-art for HTS-based SQUIDs. For this purpose, we have followed the fabrication steps for several samples and observed their electrical and transport behavior, with relation to the already known models, such as the Resistively Shunted Junction (RSJ).

The optimization work divides in: in-situ modifications, introduced therefore during fabrication, and ex-situ techniques, conducted after fabrication of the devices. By in-situ modifications, we refer in this context to variations of parameters of the fabrication process and, specifically of the carbon mask and etching steps, which are the most relevant for the specific outcome of the GDBs.

By ex-situ techniques, we refer to electromigration (EM), in particular DC and AC EM. Here, the results of this technique applied on weak links are still at their early stages, but show very promising improvements on the electrical properties of the SQUIDs. Voltage modulation depth, ΔV , increments of up to 8 times the original value were registered, with a strong dependence found on the shape of the constriction through which the current was sent. These findings suggest that EM would be instrumental to consistently improve *a posteriori* the magnetic flux sensitivity of nanodevices such as GDB-based SQUIDs.

Keywords: HTS, YBCO, GDB, optimization, SQUID, EM, AC-EM

Abstract in lingua italiana

Il lavoro presentato in questa tesi si concentra sull'ottimizzazione di nanostrutture fabbricate in YBCO, un superconduttore ad alta temperatura (HTS), e specificatamente su Groove Dayem nanobridges, con lo scopo di costruirci dispositivi superconduttori basati sull'interferenza quantistica (SQUIDs). Infatti, nanostrutture in YBCO sono al centro della ricerca nel campo di sensori superconduttori, come nel caso di magnetometri ultrasensibili, per via dei vantaggi che implementare un materiale HTS porterebbe alla ricerca ed all'aspetto più commerciale di queste tecnologie. In questa tesi, lo scopo è stato di fabbricare e migliorare la sensibilità al flusso magnetico di SQUID basati su GDB nanostrutture. Di fatto, queste strutture hanno già dimostrato di dare buoni risultati per misurazioni alla temperatura di lavoro per HTS, 77 K, per quanto non ancora allo stato dell'arte. Per questo proposito abbiamo seguito la fabbricazione di svariati campioni ed valutato la loro risposta in proprietà elettriche e di trasporto, con il supporto dei modelli relativi a questi dispositivi già conosciuti, come il RSJ.

Il lavoro di ottimizzazione in sé, invece, si è diviso in due parti principalmente: modificazioni in-situ, introdotti durante la fabbricazione, e tecniche ex-situ, perciò condotte sui dispositivi dopo la loro fabbricazione. Nello specifico, con modificazioni in-situ, ci si riferisce a parametri che abbiamo variato durante il processo che, nel nostro caso, riguarda soprattutto la maschera di carbone ed in processo di incisione nel YBCO, che abbiamo trovato essere i più rilevanti per i risultati su GDB.

Per tecniche ex-situ invece ci si riferisce all'elettromigrazione, che si divide in DC ed AC. Rispetto all'applicazione dell'elettromigrazione, la tecnica è ancora ai suoi stati iniziali, ma già mostra risultati molto incoraggianti. Incrementi nelle modulazioni di voltaggio fino ad anche 8 volte il valore iniziale sono stati trovate, con una forte correlazione con lo specifico profilo delle costrizioni del dispositivo. La presenza e la positività di questi risultati suggerisce di conseguenza la possibilità di implementare sempre uno stadio di elettromigrazione a posteriori della fabbricazione, per incrementare la sensibilità dei dispositivi al loro massimo.

Parole chiave: HTS, YBCO, GDB, ottimizzazione, SQUID, elettromigrazione

Contents

Abstract	i
Abstract in lingua italiana	iii
Contents	v
Introduction	1
1 Background	3
1.1 Superconductivity	3
1.1.1 High Temperature Superconductors	7
1.1.2 YBCO	8
1.2 HTS-based nanostructures	12
1.2.1 Josephson Effect	13
1.2.2 SQUID: overview and working principle	15
1.3 YBCO-based JJ and weak links	17
1.3.1 Nanowire based SQUIDs: Dayem Bridge and GDB	19
2 GDB-based SQUIDs fabrication process	27
2.1 Growth and characterization of YBCO thin films	27
2.1.1 YBCO deposition and optimization of process	28
2.1.2 Characterization of YBCO surface and properties	30
2.2 Fabrication	33
2.2.1 GDB nanopatterning process	33
2.3 Carbon mask deposition	37
2.4 Ion Milling process: etching of the mask	38
3 Characterization of SQUID properties	41
3.1 GDB-based SQUIDs: characterization of electronic properties	42
3.2 Optimization of GDB-based SQUIDs	47

4	Tuning of GDB electrical properties	53
4.1	Electromigration: tuning of Oxygen doping	53
4.2	Electromigration tuning of nanowire-based SQUID devices	56
4.2.1	Electromigration tuning of GDB-based SQUID devices	60
5	Conclusions and future developments	65
	Bibliography	67
	List of Figures	73
	List of Tables	75
	List of Symbols and Abbreviations	77
	Acknowledgements	79

Introduction

High Temperature Superconductors (HTS) hold researchers interest since their discovery. The mysteries connected to their fundamental physics, in fact, are all but solved and, since their discovery, have increased in complexity. The many inter-playing orders and lack of a comprehensive theory able to explain both HTS and Low Temperature Superconductor (LTS), makes this field one of the more studied in condensed matter physics. Cuprates, and $\text{YBa}_2\text{Cu}_3\text{O}_{7-\delta}$ (YBCO) in particular, have demonstrated to be very challenging materials to understand. From their discovery, more than 30 years ago, they have been extensively investigated, and yet new phenomena of charge and stripe ordering continue to give unexpected results. But alongside with the theoretical interrogatives, studies on HTS for technological applications are very active as well. Their discovery has opened up huge possibilities of improvement on many LTS-based technologies, by extending their working range to higher fields and higher temperatures.

Superconducting QUantum Interference Devices (SQUIDs) are among the most prominent of those technological applications. Currently used in a vast number of fields, from magnetic field sensing in biomagnetism to scanning microscopy, SQUIDs have many reasons to attract attention in the research field. Therefore, it is beneficial for many applications to fabricate HTS-based SQUID, instead of LTS, to extend their working range. However, mostly due to the higher level of noise found in HTS measurements, HTS-based SQUIDs, while being functional, do not reach yet the performances obtained with LTS-based ones. Thus, the improvement of HTS-based SQUIDs performances requires a fine optimization of the components of such devices. The most determining of which are the Josephson Junctions (JJ).

Different alternatives are currently available for implementing JJs in HTS SQUIDs, the most performing of which is the Grain Boundary (GB). It requires however a long and costly fabrication, that doesn't hold the best reliability. Another option that was recently presented is the Groove Dayem Bridge (GDB). While it is not yet competitive to GB in terms of performances, it has given promising results and can be hopefully optimized to reach the state-of-art.

The aim of this thesis has been, therefore, to improve on the work done on GDB-based YBCO SQUIDs and, while doing so, to test the limits to which the transport properties of these nanostructures could be pushed, both with fabrication and ex-situ techniques.

The first chapter presents an overview on the physical background of superconductivity, YBCO and a close-up on HTS based devices; the second chapter describes the fabrication process done in order to obtain GDB-based SQUIDs and its fundamental steps, with particular focus on the process steps that were most crucial to optimize the weak links.

The third chapter focuses on the general transport properties of these devices, where explanations will be corroborated with some of the results that were found during this work, followed in the end by the results obtained from the optimization of the aforementioned steps of the fabrication process.

The last chapter will contain the bulk of the experimental results to be presented: the electromigration of weak links, starting with the results obtained on bare nanowires, followed by the ones achieved on GDB-based SQUIDs.

The final one presents the conclusions of this work and what was achieved, plus considerations on possible future developments.

1 | Background

In the following will be presented a discussion on superconductivity, high temperature superconductors (HTS) and relevant models, with particular attention to the key concepts for this thesis work. Afterwards, a short summary on $\text{YBa}_2\text{Cu}_3\text{O}_{7-\delta}$ (YBCO), the HTS base material for this work, will be given and lastly technological applications for HTS will be overviewed.

The emphasis in the technological applications will be, of course, on HTS-based Superconducting QUantum Interference Devices (SQUIDs), specifically, nanowire-based ones, which will be the main focus for the rest of the thesis as well.

1.1. Superconductivity

In first approximation, the superconductivity phenomenon can be simply characterized by two distinct properties: perfect conductivity and perfect diamagnetism, both appearing at the same time inside a material, when it is brought below a specific temperature. The first means that the material has zero electric resistance, which implies that a current can flow through it without inducing any voltage drop and therefore without any energy loss. This was first reported in 1904 by Camerling Onnes, when he noticed a drop in the resistance of Mercury, when it was brought below 4.2 K [1].

This specific temperature, which defines the point at which the material transitions from the normal state to the superconductive one, is called critical temperature, T_c , and it was found to be an intrinsic property of the material itself.

Perfect diamagnetism, instead, was found much later in 1933 by Meissner, hence the alternative name of Meissner effect, and refers to the tendency of a superconductor (SC) when below T_c to expel any externally applied magnetic field from its bulk, as long as its value is below a critical field B_c [2]. Perfect diamagnetism is what discriminates between a SC and a "trivial" perfect conductor, which will present zero resistance, but won't expel any external pre-existing field when transitioning to zero resistance.

Following these experimental discoveries, the first model for superconductivity was pro-

posed by the London brothers, Fritz and Heinz [3], who developed, although still in an intuitive way from the noticed phenomena, the two following equations

$$\partial_t \vec{J}_s = \frac{n_s e^{*2}}{m^*} \vec{E} \quad (1.1)$$

$$\vec{\nabla} \times \vec{J}_s = \frac{n_s e^{*2}}{m^*} \vec{B} \quad (1.2)$$

where \vec{J}_s is the superconducting current density and n_s is the density of superconducting electrons which flow without dissipation. These equations relate the current in a superconductor to the electromagnetic field and manage to describe in this way the two aforementioned hallmarks of superconductivity. The London equations describe the superconducting system as a two-fluid system, where the first fluid represents the normal, resistive electrons, and the second the superfluid, which appears under T_c , and is formed by "special" electrons, described to have an effective mass $m^* = 2m_e$ and charge $e^* = 2e$. Equation (1.1) introduces the perfect conductivity, for which the superfluid is accelerated by the electric field inside the material, not following Ohm's Law as for electrons in metals, and if there is no electric field, a dc-current can still flow without voltage drop. Equation (1.2), instead, explains the Meissner effect, which can be more easily understood when combined with Ampere's law, to obtain:

$$\nabla^2 \vec{B} = \frac{1}{\lambda_L^2} \vec{B}, \quad \lambda_L \equiv \sqrt{\frac{m^*}{\mu_0 n_s e^{*2}}} \quad (1.3)$$

with μ_0 being vacuum permeability. The magnetic field is screened completely in the bulk of the material due to the presence of screening currents flowing in a thin region at the surface of the superconductor. Both the field and the related screening currents decay exponentially into the bulk of the superconductor from its surface, with a characteristic length scale λ_L , which is known as the London penetration depth.

After the London equations, the next important step in understanding the superconductivity phenomenon was achieved in 1950, with the model developed by Ginzburg and Landau (GL) [4]. They postulated a phenomenological model, based on Landau's theory of second-order phase transitions, which introduces a spatial dependence to the superfluid density, $n_s(\vec{r})$, and an order parameter for the superconducting transition, which is described with the following complex wavefunction:

$$\Psi(\vec{r}) = |\Psi(\vec{r})| e^{i\phi(\vec{r})} \quad (1.4)$$

And where $|\Psi(\vec{r})| = \sqrt{n_s(\vec{r})}$ is the relation to the superfluid density and $\phi(\vec{r})$ is the phase, which is a function of the position as well.

This theory was built for temperatures close to the critical one, where the superconducting transition happens, and where the order parameter is assumed to be small and slowly varying in space. Therefore, the free energy of the superconducting system, $F = F(\Psi, T)$, which is immersed in a magnetic field, can be expanded in series of Ψ and $\vec{\nabla}\Psi$:

$$F = F_n + \alpha|\Psi|^2 + \frac{\beta}{2}|\Psi|^4 + \frac{1}{2m^*}|(-i\hbar\vec{\nabla} - e * \vec{A})\Psi|^2 + \frac{\vec{B}^2}{2\mu_0} \quad (1.5)$$

Where F_n is the free energy of the normal phase, $\alpha = \frac{\partial F}{\partial n_s}$ and $\beta = \frac{\partial^2 F}{\partial n_s^2}$ the temperature dependant parameters and \vec{A} the magnetic vector potential.

By minimizing the free energy in eq. (1.5) with respect to the variations both in the order parameter and in the vector potential we can find the equilibrium wave function. As a result the two Ginzburg-Landau (GL) equations are obtained:

$$\alpha|\Psi|^2 + \frac{\beta}{2}|\Psi|^4 + \frac{1}{2m^*}(-i\hbar\vec{\nabla} - e * \vec{A})^2\Psi = 0 \quad (1.6)$$

$$\vec{J}_s = \frac{\hbar e^*}{2im^*}(\Psi * \vec{\nabla}\Psi - \Psi\vec{\nabla}\Psi^*) - \frac{e^{*2}}{m^*}\vec{A}|\Psi|^2 \quad (1.7)$$

where we have the following boundary condition $(-i\hbar\vec{\nabla} - e * \vec{A})\Psi|_n = 0$, assuring that no current flows out of the superconductor surface n . From the first GL equation, a second characteristic length can be found, besides λ_L , which represents the distance at which the order parameter can vary without the system undergoing an energy increase, the coherence length ξ :

$$\nabla^2\Psi = \frac{\Psi}{\xi^2}, \quad \xi \equiv \sqrt{\frac{\hbar^2}{2m^*|\alpha|}} \quad (1.8)$$

This equation is obtained from (1.6), solved with negligible external magnetic field and very small value of Ψ just above the transition temperature. It describes the exponential decay of Ψ over the length scale determined by the coherence length.

However, the GL theory is still a phenomenological one and for a successful microscopic description of the mechanism of superconductivity we need to wait until 1957, when Bardeen, Cooper and Schrieffer (BCS) proposed a model centered around the pairing of electrons [5]. Indeed, after Maxwell observed in 1950 the Isotope effect for Hg, which suggested a correlation between electron-phonon coupling and superconductivity, they theorized that, while electrons normally repel each other due to the Coulomb interaction, in certain conditions a weak attractive force may form between them, such that for those close to the Fermi surface it may overcome the Coulomb repulsion. This force would be mediated by phonons and would create, for temperatures below the critical one, spin singlet pairs, the so-called Cooper-pairs.

While electrons normally are fermions, i.e. they have half integer spin value, thus for the Fermi-Dirac statistics are forbidden to occupy the same quantum state, Cooper pairs, being the sum of two half integer spins, are effectively bosons, and can therefore occupy the same state. After formation, Cooper-pairs would condense into the same ground state, which can be described by the wavefunction in (1.4). According to the BCS theory, for temperatures below $T < T_c$, it is energetically favorable for electrons to form Cooper-pairs, where the binding energy of one pair is the superconducting energy gap 2Δ , with $\Delta \simeq 2\hbar\omega_D e^{-1/N(E_F)g_{eff}} \simeq 1.76k_B T_c$, being a property of the specific material and where ω_D is the Debye frequency, $N(E_F)$ the electron density of states at the Fermi energy and g_{eff} the effective electron-phonon coupling.

This last theory is successful in describing the superconductivity phenomenon at low temperatures and is therefore sufficient for describing those superconductors that have very low critical temperatures (Low Temperature Superconductors, LTS), such as Nb with $T_c = 9K$ and its alloys, or Al with $T_c = 1.2K$, etc. However, these are not the only type of superconductor that was discovered. In fact, in 1986, Bednorz and Müller reported superconductivity at much higher critical temperatures (around 77-90 K) in a class of materials called *cuprates* [6]. That, if we restrict ourselves to the BCS theory, should have not been possible, since the theory predicts the maximum possible critical temperature to be $T_c = 32K$. That, and several other incongruities, show how BCS, while being the very first microscopic theory for superconductivity, is not a comprehensive theory and is not, as matter of fact, able to explain the so-called High Temperature Superconductors (HTS), of which YBCO, the compound at the center of this work, is one of the most known and studied.

1.1.1. High Temperature Superconductors

High Temperature Superconductors (HTS) are a class of materials of relatively recent discovery (less than 40 years), and are, by the most general description, materials which exhibit superconducting behavior at temperatures much higher than LTS materials.

The much higher temperature at which HTS transition to the superconductive state, well above the liquid nitrogen (N_2) boiling point $T = 77K$ is inexplicable with BCS theory and the true microscopic origin of their superconductivity is actually still subject of studies as today.

However, the high critical temperature is not the only parameter that distinguishes HTSs from LTSs. First of all, while LTSs are usually metals, HTSs are more often oxide ceramic materials, therefore with a much more complex crystal structure and where their superconducting properties are strongly related to their charge doping. Moreover, they usually present very different values for λ, ξ and Δ with respect to what is found for "ordinary" superconductors.

Given the expression for Δ , since it is proportional to T_c , the energy gap for HTS will be much bigger, as well as the London penetration depth will be larger, due to a lower carrier concentration, while the coherence length will be much smaller. This is related to the fact that all HTS are type II SCs, while most LTS are type I.

SCs can indeed be divided into two categories, type I and type II, depending on the ratio λ/ξ . If this is lower than $1/\sqrt{2}$, the SC will be defined as a type I and will in general have small penetration length of the external magnetic field inside the material bulk and a sufficiently large coherence length for the order parameter. This implies that for a type I superconductor, if the external field B_e exceed the critical field of the material H_c , superconductivity is broken and the normal state reconstituted. What instead happens with a type II SC is quite different. In this second case ($\lambda/\xi > 1/\sqrt{2}$), the material has two different critical fields, $H_{c,1}$ and $H_{c,2}$, when B_e exceeds the lower one, $H_{c,1}$, but not the higher one $H_{c,2}$, the material's superconductivity does not break, but transitions into the so-called mixed state, or the Abrikosov regime. In this regime, some of the external field enters the material bulk and constitutes what is known as Abrikosov vortices (also referred to as fluxons) [7]. Here, Ψ is locally suppressed, over a length scale equal to ξ , which forms the normal core of the vortex. A supercurrent circulates around the core, which decays into the SC over a length scale equal to λ_L . The total magnetic field over the vortex area (both externally applied and generated by the supercurrents) equals exactly *one flux quantum* $\Phi_0 = h/2e$. When $H_{c,2}$ is reached by the external field, superconductivity is completely broken and the material goes back into the normal state, but it is worth

noticing that usually $H_{c,2} > H_c$.

The presence of this mixed state, in which superconductivity is still good enough for most applications, together with the much higher critical temperature, that consents the use of N_2 as a cooling mechanism instead of liquid He , makes HTSs very important materials for technological applications in different fields, for example magnetic field sensing. Not only this, but the current lack of a microscopic theory for HTS superconductivity and the correlation they show to have between the charge doping level and their physical property makes them vastly interesting also from a research point of view. Between all known HTSs, as previously mentioned, cuprates were the first discovered and one of the most used in technological applications. In the next section, the focus will be on YBCO, one of the most studied materials belonging to the cuprates family and the one that was the base for this thesis work as well.

1.1.2. YBCO

YBCO is an oxide ceramic material belonging to the cuprates family and a schematic representation of its crystal unit cell is shown in Fig. 1.1.

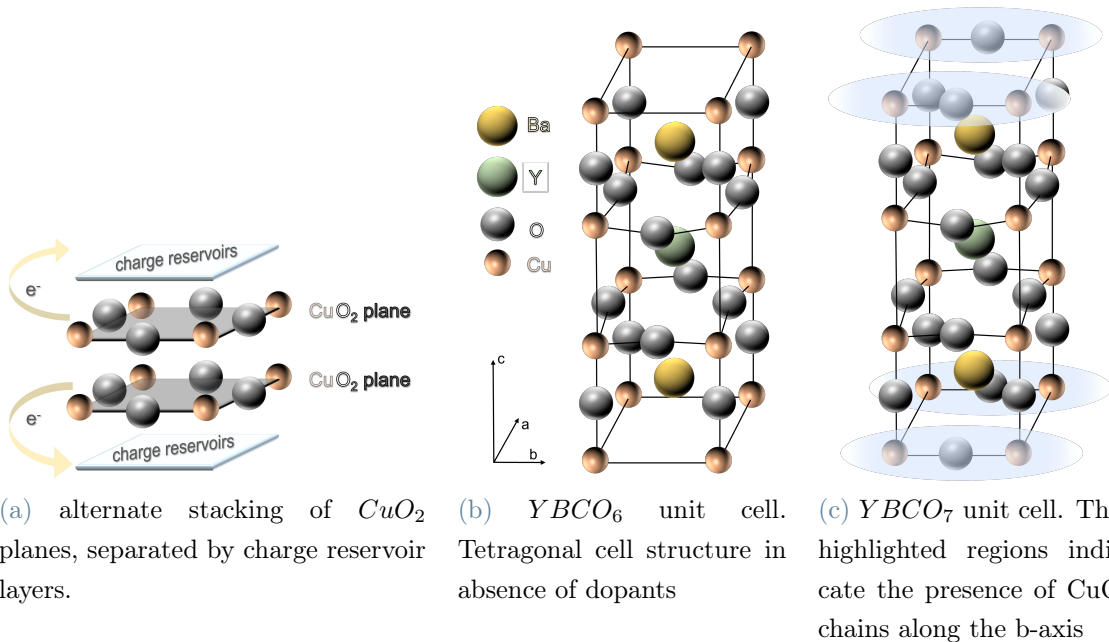


Figure 1.1: Schematics of a YBCO unit cell crystal structure. Hole doping is represented by the transfer of electrons from the CuO_2 planes to the charge reservoirs. Adapted from [8]

As all the cuprates, it presents a quasi-two-dimensional layered structure, that contains

one or more CuO_2 planes for unit cell. In the particular case of YBCO, the unit cell is composed by three perovskite cells, separated by two CuO_2 planes, which results in a strong anisotropy of this structure's properties between the in-plane (a- and b-axis) and the out-of-plane (c-axis) direction.

In absence of dopant atoms (Fig. 1.1, b) the cell structure is tetragonal, i.e. the a and b lattice parameters are the same [9]; in this configuration YBCO is a Mott insulator [10]. When oxygen atoms are added to the compound (hole doping of YBCO's CuO_2 planes), we have the formation of CuO chains along the b-axis, as shown by the highlighted regions in Fig. (1.1, c).

The CuO chains act in this context as "charge reservoirs" for the CuO_2 planes, meaning that they receive electrons from them. This results in a hole doping of the planes, which become the main sites for electrical conduction [11]. The formation of these chains due to the additional oxygen on the planes results in a deformation of the YBCO unit cell as well, which goes from being tetragonal to an orthorhombic crystal structure. This implies that it becomes anisotropic and elongated also along the b-axis, which leads to an anisotropy of the superconducting properties between the a-axis and the b-axis [12], even if on a lower scale if compared to the anisotropy along the c-axis.

The level of hole doping (amount of oxygen vacancies) is given by the parameter δ and plays a key role in determining the physical properties of the material. While undoped YBCO is insulating at all temperatures, as holes are introduced in the CuO_2 the character of the material becomes much more varied and complex and, as of now, still under intense study.

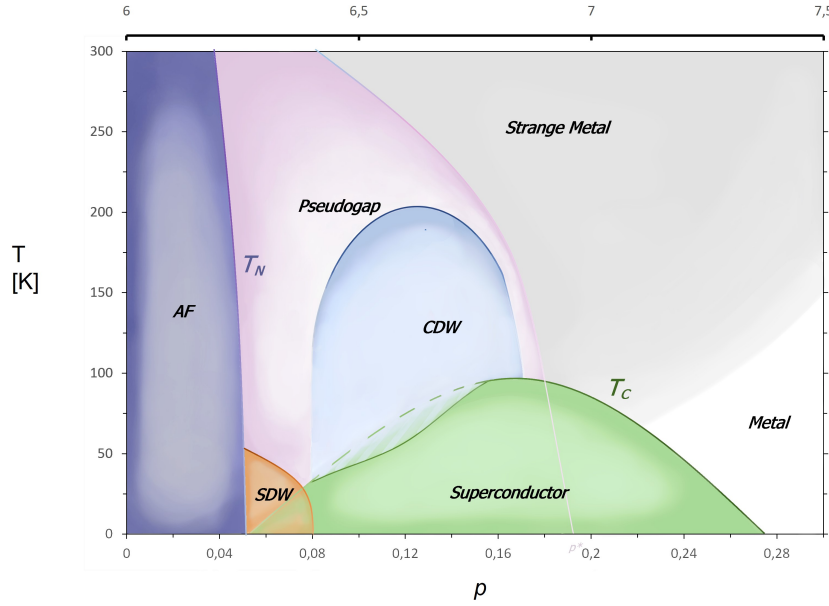


Figure 1.2: Phase diagram of YBCO. Adapted from [13]

Below is shown a schematic summary of the phase diagram of YBCO, showing the material properties at different temperature, T , and doping level, commonly expressed as p , which is the number of holes per planar Cu atom. It is worth pointing out that between p and $7 - \delta$, the amount of oxygen in the YBCO unit cell, there is a non-linear relation [14].

As it can be seen from Fig.1.2, the diagram is very complex and presents several intertwined electronic orders, in addition to superconductivity, which is however the focus for most of the current technological application of YBCO, such as SQUID magnetic sensors.

In the remainder of this section, we will briefly explore the phases present in the diagram for YBCO.

Superconductivity: In YBCO, superconductivity is present in the doping range $0.05 < p < 0.27$ and the curve delimiting the behavior, $T_c(p)$, is a parabolic one with the maximum in $T_c = 93K$ for p value close to 0.16. Depending on p value, the samples of YBCO will be referred to as *underdoped*, *optimally doped*, *overdoped*, which corresponds respectively to $p < 0.16$, $p = 0.16$ and $p > 0.16$ [14]. For $p = 0.16$, the unit cell lattice parameters will be $a = 3.82$, $b = 3.89$ and $c = 11.69$ [15]. $T_c(p)$ deviates from parabolic behavior for $p \approx 0.125$, where it is suppressed by up to 20 K. This suppression is commonly attributed to competition with charge order, which is strongest in that doping range [16].

Strange Metal: The normal state present in correspondence to the optimally doped region is called "strange metal" [17]. In this region, we have a linear dependence of the material resistance with respect to temperature, $R \propto T$, which starts from the minimum

temperature above the superconducting dome and extends up to several hundreds of K. What we would have expected instead, would have been $R \propto T^2$, for low temperatures for a Fermi liquid, therefore for a normal metal [18]. But this behavior deviates from it, even in the absence of a saturation point of resistivity for high T. The discussion about this phase is still open, and several are the hypothesis proposed, one is that it may originate as a consequence of quantum fluctuations coming from a quantum critical point (QCP) placed at zero temperature for a p value inside the superconducting dome [13].

Pseudogap: Present on the underdoped side of the diagram and below in temperature with respect to the strange metal phase. This phase is characterized by the opening under its characteristic temperature of gaps in the Fermi surface, with similar symmetry to a superconducting order parameter with diagonal nodes [13], and the deviation of the resistance from the linear dependence with T, typical of the strange metal phase. A plethora of complicated electronic phenomena, e.g. nematicity [19], have been reported for temperatures close to the limit with strange gap, but the relation with this phase is not fully understood.

Charge order: A large portion of the underdoped side of the diagram is occupied by a charge order in the form of charge density waves (CDW) [20]. CDW is a periodic modulation of the charge density in the CuO_2 planes, it is present for circa $0.08 < p < 0.17$, and it is incommensurate with the lattice period in the case of YBCO. There is compelling evidence that the CDW competes with superconductivity. In YBCO case, these modulations appear in the underdoped regime, for $T_{CDW} > T_c$. It is still observable below T_c , but strongly suppressed. Dynamical CDW fluctuations were recently found in the majority of the phase diagram, even in the strange metal phase [21, 22].

Spin order: In the underdoped region, but above $p \approx 0.05$, the antiferromagnetic order is substituted by another spin order, called spin density wave order (SDW) [23]. SDW is a periodic modulation of the electronic spin density and it is incommensurate and uniaxial along YBCO a-axis. It is static at low T and slowly fluctuating at higher T [24].

Fermi liquid: On the overdoped side of the phase diagram, where $R \propto T^2$ is recovered. YBCO behaves as such as a metal in this region.

AF (Mott insulator) For doping $p < 0.05$, YBCO is a Mott insulator and has an antiferromagnetic properties.

The complexity reported by the phase diagram of YBCO is a good indication of the challenges that cuprates introduce in an experimental setting, when the goal is to first fabricate high-quality thin films with it and, second, structures at the nanoscale. Not

only HTSs such as this one are not monoatomic as the most common LTS, but they often contain heavy metals or exotic atoms that usually restrict the number of possible fabrication techniques which do not affect the stoichiometry of the material, changing, in this way, the region of the phase diagram in which we are operating. This means that fabrication will need to consider the risk of oxygen out diffusion, a crucial aspect for YBCO thin films, since it would immediately alter its SC properties. Beside this, cuprates, being ceramic materials, are prone to defects and brittle, which further affects the quality of the thin films and nanostructures that can be built with them. All that is presented concurs in making the fabrication much more challenging with respect to LTSs and sometimes even not reproducible.

1.2. HTS-based nanostructures

However, even when fabrication difficulties with respect to LTSs are taken into account, we find that HTSs are still of great interest in relation to structures at the nanoscale dimension. It should be in fact understandable how, given the sheer complexity and the number of unanswered questions, even after more than 30 years the cuprates are often at the center of studies. Studies that, in order to investigate their properties in conditions for which the characteristic length scales of charge ordering phenomena are approached (namely, around the coherence length, which is circa 10 nm for $p=1/8$ [16, 20]), many times require patterning of structures at the nanoscale (mesoscopic structures). But besides the attractiveness of the fundamental interrogatives on HTS, multiple technological applications do rely on them for basic functioning or for improvement with respect to LTS-based devices. And SQUID devices are one of them.

Indeed, the presence of the aforementioned mixed state delimited by usually a quite large $H_{c,2}$, and the much higher than LTS critical temperature $T_c > 77K$, opens up applications to the possibility of using liquefied nitrogen as a cooling mechanism and to a general extension of range for the working conditions of HTS devices. The possibility of using N_2 instead of liquid helium, LHe , is particularly interesting in this context, considering that, not only the necessity for LHe introduces complexity in the required equipment and experimental setup, but it is also very costly since it demands for a resource that is limited and getting less available every year. N_2 instead is much more easily stored and makes for more portable, compact devices, which is fundamental in applications that require sensing, since the distance from the source of the field should be reduced as possible to maximize the sensitivity of the system. To counterbalance these advantages, we should also take into account that nanostructures built with HTSs usually suffer from higher

noise contributions, due to the much higher temperature at which they are operated. But overcoming the limitations connected to these structures would introduce strong improvements in several technological areas that are still currently dominated by LTS-based devices, especially the sensing one.

The aim of this work is therefore to improve upon the already quite developed HTS-based device fabrication, in order to obtain the best quality nanostructures and use them as a starting point to advance in the field of YBCO-based magnetic flux sensors. In the following sections the concepts presented will be the ones specifically needed in order to better understand the working principles of a HTS-based SQUID, and therefore the needs that one encounters while fabricating one for the purpose of magnetic flux sensing.

1.2.1. Josephson Effect

Of most importance in the field of application of SCs, both Low and High temperature ones, we have the *Josephson Junction* (JJ). It was first proposed by Brian Josephson in 1962 and relies on the tunneling of Cooper-pairs that happens when a barrier is placed between two superconductors, the *Josephson effect* [25]. Indeed, when a SC is placed in contact with a normal conductor (N), its wave function Ψ extends into it, decaying exponentially. If another SC is on the other side of it and N is thin enough, SC1 and SC2 wavefunctions overlap inside the N, allowing for a flow of Cooper-pairs through it, originating the Josephson effect. JJs have been instrumental both for the study of SC properties and technological applications.

Two equations are responsible for describing the dynamics of a JJ:

$$I = I_c \sin \phi \quad (1.9)$$

Which is the DC Josephson equation, also called Current Phase Relation (CPR) of a JJ. It describes the relation between the supercurrent I circulating through the junction and the phase difference ϕ of the two SC electrodes across the barrier.

$$V = \frac{\hbar}{2e} \frac{\delta \phi}{\delta t} \quad (1.10)$$

This second equation is instead the AC Josephson equation, which relates the voltage drop across the junction to the time evolution of the phase difference ϕ . Consequence of this is that, if ϕ is constant, no voltage drop will be registered across JJ.

When a JJ employs a normal conductor (N) such as a metal for the barrier, it is usually

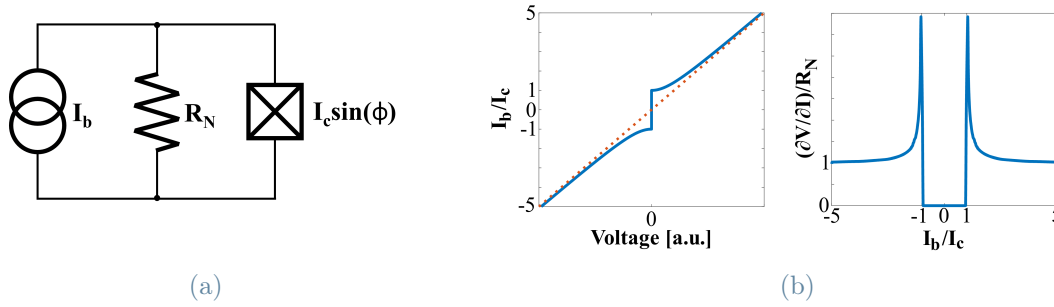


Figure 1.3: RSJ model: a) Circuit scheme for RSJ model; b) IV and dR of a JJ in RSJ model. Adapted from [26]

referred to as SNS (Superconductor-Normal conductor-Superconductor) JJ. But that is not the only option for a JJ. For example, a SIS JJ is built when an insulator (I) is used as separator. Alternatively, the Josephson effect can be realized with structures called weak links. Many are the options for this last type of JJ, but most commonly a weak junction will be a SS'S JJ. In this case, separating the two identical SCs there is another SC, S', which however presents different superconducting properties with respect to S. This is usually done by placing a superconductor with lower critical temperature or by introducing a geometrical constriction, reduction of dimensions with respect two the two SCs on the sides, usually referred to as electrodes.

RSJ model

For most application is usually useful to describe JJs with respect to their Current-Voltage characteristic (IVc), i.e. the relation that ties current through the junction to voltage across it. A JJ is usually characterized by applying a bias current I_b and measuring the resulting voltage drop V . While for $I_b < I_c$ the Josephson equations are valid and predict $V = 0$, for $I_b > I_c$ the voltage drop changes and needs to be calculated with the Resistively Shunted Junction (RSJ) model. A schematic view of it is presented in Fig. (1.3, a)). For $I_b > I_c$, the voltage of the JJ is obtained by solving the circuit depicted, where we interpret the JJ above I_c as a parallel between the JJ under I_c and a resistor R_N , which represents the normal state resistance of the junction.

For simplicity, the resistance of the normal state is assumed to be ohmic, hence independent of V . This will imply that the total current flowing through the junction could be expressed as:

$$I_b = I_c \sin(\phi) + \frac{V}{R_N} = I_c \sin(\phi) + \frac{\hbar}{2eR_N} \frac{d\phi}{dt} \quad (1.11)$$

Where we have also used eq.(1.10) for V . By integrating over time, we reach than the following expression for the average voltage:

$$\langle V \rangle = R_N \sqrt{I_b^2 - I_c^2} \quad (1.12)$$

While for $I_b < I_c$, we have a superconducting state, hence $\langle V \rangle = 0$. In Fig. (1.3,b) the IVC and the differential resistance $\delta V/\delta I$ of a RSJ are shown. From it we can derive that, when I_b is brought just above I_c , the voltage undergoes a very rapid increase and generates a peak in the differential resistance, much higher than the normal resistance R_N , shown with the red dotted line. By continuing to increase the bias, we end up recovering R_N value, implying that in that regime a RSJ behaves similarly to a linear resistor with R_N resistance.

This model is found to usually work quite well for SNS type of junctions, while junctions as the SIS require the application of the full model, the Resistively and Capacitance Shunted Junction (RCSJ) model, of which RSJ is just a special case.

1.2.2. SQUID: overview and working principle

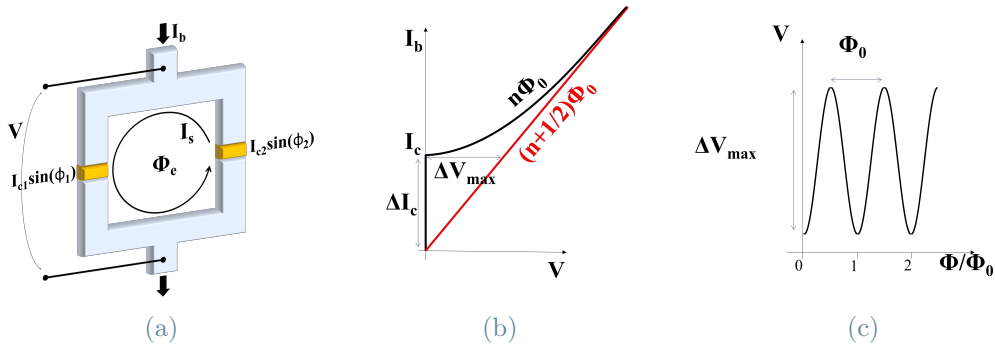


Figure 1.4: SQUID working principle: a) A dc SQUID superconducting loop, biased with I_b ; b) IVC curve, with focus on critical current modulations with respect to integer multiples of flux and half-integers; c) Voltage depth modulations with respect to the flux. Adapted from [26]

Superconducting QUantum Interference Devices (SQUIDS) are one of the most prominent applications of SCs. Simply speaking, a dc SQUID consists of two JJ connected in parallel on a superconducting loop, as shown in the picture 1.4 [27], as opposed to a rf SQUID, which involves only a single JJ in the superconducting loop. For our purposes, we are interested only in dc SQUIDS. The working principle of a SQUID is the following: when

we have a magnetic flux Φ_e through the loop, changing monotonically, the maximum supercurrent I_c^{max} that the SQUID can sustain is modulated with a period of one flux quantum, $\Phi_0 \equiv h/2e$. Provided that IVC follows the RSJ model, this modulation results in a concomitant modulation of the voltage across the SQUID, when the device is biased with $I_b > I_c^{max}$, has shown in Fig. 1.4, b). This behavior essentially makes of the SQUID a flux-to-voltage transducer, with a transfer coefficient determined by $\delta V/\delta\Phi$, as can be seen in Fig. 1.4, c). More in detail, when a SQUID is biased with a dc current $I_b = I_{SQ}$, we have that:

$$I_{SQ} = I_{c,1} \sin(\phi_1) + I_{c,2} \sin(\phi_2) \quad (1.13)$$

Where $\phi_{1,2}$ are the phase differences across the two weak links. These have to respect the quantization of flux around the SC loop:

$$2\pi n = \phi_1 - \phi_2 + 2\pi \frac{\Phi}{\Phi_0} \quad (1.14)$$

where Φ_0 is the aforementioned flux quantum and $\Phi = \Phi_e + L_{SQ}I_s$ is the effective magnetic flux through the SC loop, i.e. the sum of the external magnetic flux, Φ_e , and the flux generated by the superconducting currents I_s circulating in the loop times the loop inductance L_{SQ} . By using the expression for ϕ_1 in eq.1.14, with negligible loop inductance, back into eq.1.13 and by assuming symmetric junctions ($I_{c,1} = I_{c,2}$), we obtain for the current of the SQUID:

$$I_{SQ} = 2I_{c,1} \left| \cos\left(\pi \frac{\Phi_e}{\Phi_0}\right) \right| \sin(\phi) = I_c(\Phi_e) \sin(\phi) \quad (1.15)$$

We can therefore conclude that a dc SQUID behaves as a single JJ with a critical current $I_c(\Phi_e)$ that depends on the external magnetic flux. As a consequence, there will be a maximum for I_c , I_c^{max} , that is reached for multiple integer values of Φ_0 for the external field, and it modulates down to 0 for half-integer multiple values of it. We can establish from that that the critical current modulation depth is $\Delta I_c = I_c^{max}$.

When L_{SQ} is introduced back into the calculation, the effective value of ΔI_c is decreased, and $I_{SQ}(\Phi_e)$ value needs to be obtained through numerical calculations [28, 29]. The effect coming from the presence of a loop inductance can however be simply taken into account through the screening parameter:

$$\beta_L = \frac{L_{SQ} I_c^{SQ}}{\Phi_0} \quad (1.16)$$

Where larger values of β_L will imply a smaller modulation depth [26]. β_L becomes this

way one of the factors to be considered when evaluating the SQUID flux-to-voltage efficiency, being it inversely proportional to the amplitude of current and, therefore voltage, modulations of the device. Another way to express it will be: $\Delta I_c \simeq \frac{1}{\beta_L+1}$ [29, 30] In applications for flux sensing, the device is usually biased just above I_c and the voltage drop ΔV is measured, which is expected to be a sinusoidal voltage signal (Fig. 1.4,c).

From the voltage response to an external flux applied, we may retrieve the sensitivity of the device. The working point will be for maximum sensitivity, $V_\Phi = \max(\delta V/\delta\Phi)$, which can be approximated as $V_\Phi \simeq (\pi\Delta V_{max}/\Phi)$, where ΔV_{max} is the maximum voltage modulation depth, which is obtained at the working point. ΔV_{max} may be approximated as $\Delta V_{max} = \Delta I_c\delta R$ where we define $\delta R = \delta V/\delta I$ as the differential resistance at the working point. Sensitivity can be then expressed as $V_\Phi \simeq (\pi\Delta I_c\delta R/\Phi)$, from which we understand that in order to optimize the sensitivity of a SQUID device, we need to increase the product between the differential resistance and the critical current modulation depth.

It is worth to notice that the performance of a device relies on its noise properties as well. In this case, we find two main noise contributions: $1/f$ flicker noise and white noise. The flicker noise of SQUID is usually generated by either critical current fluctuations or thermal activation of vortices, and by taking precautions such as bias reversal scheme [31, 32], and active field cancellation [33], its effect may be mitigated to the point of being lower than white noise for all frequencies above 10 Hz (for an optimized system) at 77 K, creating as a result a "knee"-like curve of the noise. White magnetic flux noise, $S_\Phi^{1/2}$, instead, is usually the limiting factor for SQUID performances. It comes from the Johnson-Nyquist noise in the JJs and the input voltage of the preamplifier and, to be minimized, it requires for $\beta_L \equiv 1$ [34] and for ΔI_c , R_N and δR to be maximized [26]. Since the last two are tied and $\Delta V_{max} = \Delta I_c\delta R$, it is clear again how this two parameters can give a good indication of the performance of a SQUID.

1.3. YBCO-based JJ and weak links

As it will be seen later, cuprates are too complex materials to be deposited with most of the techniques usually used for LTS and, due to the very small coherence length, it is very difficult to create JJs by placing other materials as barriers between them. In fact, the superconducting order parameter for these materials can drop within just a few nm and one would need extremely accurate techniques and to have atomic clean interfaces in order to have Ψ overlap. Given however the advantages expected by substituting LTS with HTS in applications, alternative solutions have been proposed in order to fabricate the JJ, and hereby are reported the most successful ones for YBCO:

Grain Boundary: A grain boundary (GB) is a disordered region at the interface between grains with different crystallographic orientations. At this interface we have a strong suppression of the superconducting properties and it can, therefore, be used as a barrier for fabrication of YBCO JJs [35]. GBs can be obtained in multiple ways:

1) Bicrystal [36], where the substrate on which YBCO is grown is obtained by bonding together two crystals with different crystallographic orientations. As such, the YBCO thin film takes different orientations on the two sides of the bicrystal during deposition. This implies that a GB is formed along the interface where the YBCO film changes orientation. The properties of the weak link will be tuned by modifying the relative orientations of the substrate's two crystals.

2) Step-Edge [37], in which the substrate is etched to create a sloped step on which YBCO will be grown and a GB will form between the upper and lower edges of the step.

3) Biepitaxial [38], where an epitaxially grown seed layer is patterned on the substrate and it is used to change the growth orientation of YBCO over it, with respect to where the seed layer is not present. A GB is formed between these two areas.

GB-based JJs are the state-of-the-art for fabrication of YBCO JJs [39, 40]. This technology allows to obtain very high quality JJs, to the price however of a very lengthy fabrication and therefore higher costs with respect to other methods of fabrications for JJ. Moreover, methods such as the bicrystal have a fixed position for the GB, which limits design flexibility and can render the device unusable in case there are inhomogeneities along the GB line.

Ion irradiated:

YBCO can be locally damaged by exposition to a highly energetic ion beam. By doing so, we can create a region of suppressed superconductivity in which SC properties depend on the irradiation dose that was used [41]. The best results for this type of technique have been obtained with the Focused Ion Beam (FIB) technique [42]. A flow of ions, focused into an extremely narrow beam, down to a diameter of 0.5 nm (for He ions), is used to "write" over the YBCO thin film. Being the beam so narrow, this technique is able to damage very controlled areas and has, as a consequence, the advantage of being much more flexible than GB technology. Both SIS and SNS can be obtained by tuning the dose of the beam [42]. FIB may be used to create the weak link as well as an extra refining step for a pre-existing one. Due to the beam spot being so small, however, this techniques is time consuming for large exposition areas. Lastly, it performs better at temperatures lower than 77 K, requiring therefore for a lower temperature cooling mechanism than N_2 .

Nanobridges:

Another successful method to obtain YBCO weak links is to generate a constriction at some point of the material, such that the SC properties in that area of thin film will be different from the ones in the bulk. This can be achieved by narrowing down a section of the thin film along at least two of the dimensions and form there a so-called nanobridge. Belonging to this category, we find the Dayem nanoBridges (DBs) [43], or bare nanowires, in which the thickness of the film is maintained, and the Groove Dayem nanoBridges (GDBs) [26], that could be seen as an improvement on the DBs in which a nanogap is etched into the bare nanowire. Thanks to the current state of nanofabrication development, pristine nanobridges as small as $50 \times 50 \text{ nm}^2$ can be achieved that conserve bulk-like SC properties [44]. While this method requires less fabrication steps with respect to GB-based devices, we are not yet able to achieve the same performances as with GB JJ. Indeed nanowire-based SQUIDs usually present higher flux noises, especially at 77 K, and not enough I_c modulation depth to compensate for it. However, they are much more flexible in the placement and have higher reproducibility rate, since thin film defects will affect in a debilitating way only a low number of devices and the critical currents of nominally identical devices have usually a spread around 10/15 % [44].

1.3.1. Nanowire based SQUIDs: Dayem Bridge and GDB

During this work, we have focused on fabricating SQUIDs with a relatively new type of nanobridge-based weak link, the GDB weak link. But in order to better understand the physics and requirements of a similar nanostructure, here will follow a brief review on Dayem Bridges (DB) based SQUIDs and, lastly, the adaptation of it to the GDB case.

First of all, generally speaking, the SQUIDs depicted in this work would be more correctly defined as nanoSQUIDs, due to the fact that we are considering nanoscale length weak links and loop sizes in the sub- μm scale. This choice for the loop length is aimed at reducing the loop inductance, L_{SQ} and, therefore, the β_L value. Devices as such have been demonstrated to have magnetic flux noise $S_{\Phi}^{1/2}$ as low as $1 \mu\Phi_0/\sqrt{Hz}$ at 8 K [45]. Another way of improving the performances of nanoSQUIDs, is usually to reduce the thin film thickness t , since it has been demonstrated that this causes a strong increase in δR and, therefore, a strong decrease in $S_{\Phi}^{1/2}$ [46]. However, this does not work as expected, due to the fact that when t is decreased, performance gets limited by the *parasitic inductance* L_n of the nanowire. Indeed, an higher value for L_n will cause an increase in L_{SQ} and the performances of the device will, as a consequence, be strongly limited by the small modulation depth of the current δI_c .

The inductance of the nanowire divides in a *geometric* and a *kinetic* contribution. In the case of bare but narrow nanowires (DB with $wt < \lambda^2$, where w is the width of the nanowire [47]), we obtain for the kinetic inductance per unit length of the nanowire:

$$L_{kin} = \frac{\mu_0 \lambda}{\omega} \coth\left(\frac{t}{\lambda}\right) \quad (1.17)$$

where μ_0 is the vacuum permeability. We can then approximate it for a thin nanowire with length l as:

$$L_{kin} = \frac{\mu_0 \lambda^2 l}{\omega t} \quad (1.18)$$

Which implies that, for narrow nanowires, with small cross-sections, the parasitic inductance is higher and might not be a negligible contribution to the SQUID loop inductance L_{SQ} .

Therefore, we must take into account three limiting factors for the performances of nanowires: low δR , large I_c and large L_{SQ} (since they would imply a high value for β_L and low δV). While the latter, L_{SQ} , could look easily solvable by reducing the loop length, it is important to take into account the final objective for the SQUID we are fabricating. Such choice would be, in fact, detrimental in the case of a SQUID magnetometer, that requires large areas for magnetic flux sensing, as will be seen in chapter 5. Moreover, if we assume $\delta R \propto l/wt$ and $I_c \propto wt$, we would expect to maximize performances by choosing a narrow (wt small) and long (l large) wire, but such configuration would also result in an increased L_{kin} . Therefore, optimizing a nanowire dimensions consists actually in a trade-off, which sets a limit to the SQUID performance that can be achieved.

In addition, general constraints are on the dimensions chosen for weak links used as JJ, since the current-phase relationship (CPR) depends on them. In fact, nanowires may show a different electrical behavior depending on the combination of length and width values, to the point of rendering them not suitable for a JJ applications. In fact, while the Josephson effect for short one-dimensional structures was found soon after the discovery of JJs, nanowire-based weak links may often not be definable as short or one-dimensional and, in that case, our discussion needs to be extended to what happens when a nanowire's dimensions start to depart from that limit.

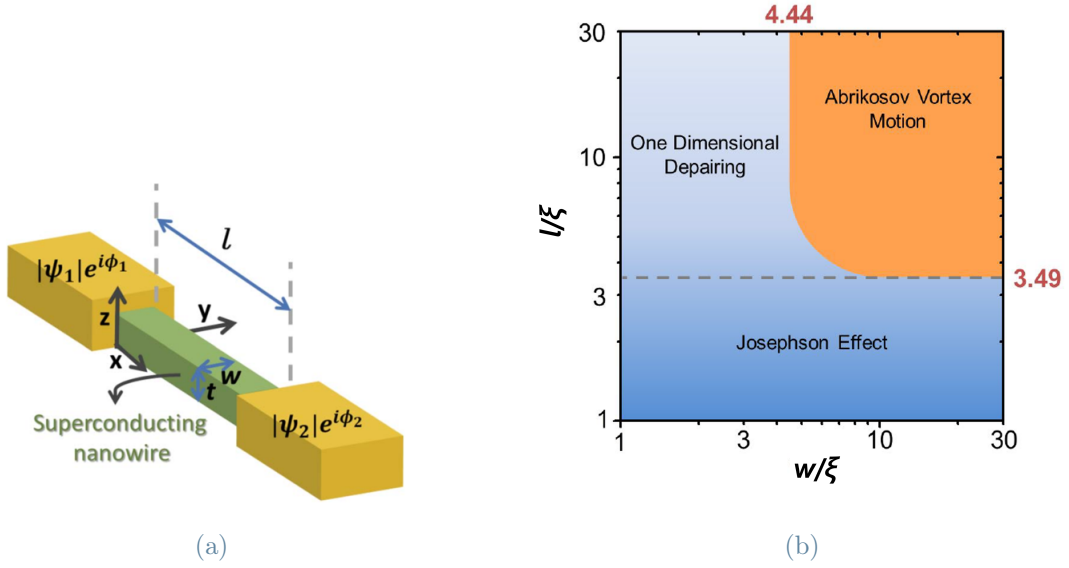


Figure 1.5: On the left, a simplified nanowire picture. On the right, a Current-Phase relationship (CPR) for YBCO nanowires, with respect to length L and width W . Adapted from [48]

As it can be seen in Fig. 1.5, with respect to the behavior of CPR, we associate particular ranges of length and width of nanowires to one of three different regions: Josephson Effect, One Dimensional Depairing and Abrikosov Vortex Motion.

In order to use weak links as JJs of a SQUID, they need to present a Josephson Effect CPR, therefore to belong in the short one dimensional wire category. We define a nanowire short and one-dimensional for $l \ll \xi$ and $w, t \ll \xi$. In this regime, the current-phase relation (CPR) is strictly sinusoidal, as for standard JJs. Considering that ξ value diverges for T close to T_c of the SC, most weak links end up belonging in this regime when T is close to the critical temperature. However, being YBCO a HTS, the coherence length ξ is very small ($\xi \simeq 2nm$), therefore YBCO short one-dimensional nanowires can be obtained only for $T \simeq T_c$. When $l < 3.49\xi$ but the width w is increased, the weak link still behaves as a canonical JJ, following the Josephson effect (single-valued CPR). True short one-dimensional nanowires ($w < \xi$) are not possible with HTS due to ξ small value.

If the length were to be increased above 3.49ξ , CPR would depart from sinusoidal behavior and become a "slanted" sinusoidal, the more is increased the ratio l/ξ . CPR would then become multivalued and be either ruled by one-dimensional depairing effect or Abrikosov vortices, depending on the width. This would result in finite voltage drops due to phase "slips" above the critical current [49] and vortex nucleations around it [48], respectively,

making the current-phase relationship much more complicated than in the Josephson effect [26].

In the case of YBCO nanowires, the typical bridge length will be around $l = 150nm$, times a minimum width $w \simeq 50nm$, therefore placing them in the short one-dimensional region only when measurements are conducted close to the critical temperature, namely at $T \simeq 85K$.

In conclusion, while DB-based weak links are less complex to fabricate with respect to GB-based and more reliable, due to their geometry they have generally far too high values of critical current density, being that around $j_c \simeq 3MA/cm^2$ at 77 K [44, 45], which implies, together with the parasitic kinetic inductance, a lower bound for β_L at around 1-3, thus limiting the performances of a DB-based SQUID [45]. If moreover the L_{SQ} contribution is included, the total screening parameter is further increased. Lastly, with respect to what is found for a SQUID with a normal weak link, well represented by the RSJ model, the current-voltage characteristics appears to show a "flux flow" type of shape [8], as the one in the following figure:

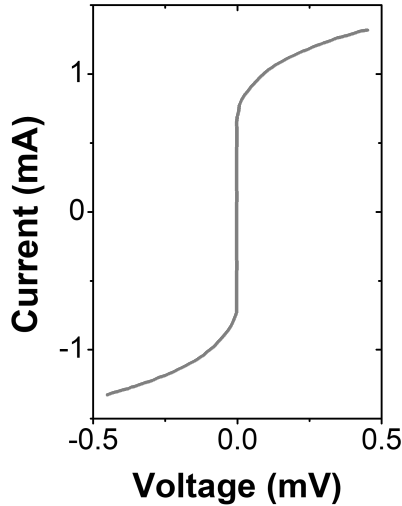


Figure 1.6: IVC for a YBCO, nanowire-based SQUID. It shows the typical flux flow behavior of a nanowire weak link. Adapted from [8]

This contrasts with optimized GDB IVCs, which will be expected to show a more RSJ-like behavior, as will be shown later in this work.

GDB-based SQUIDS

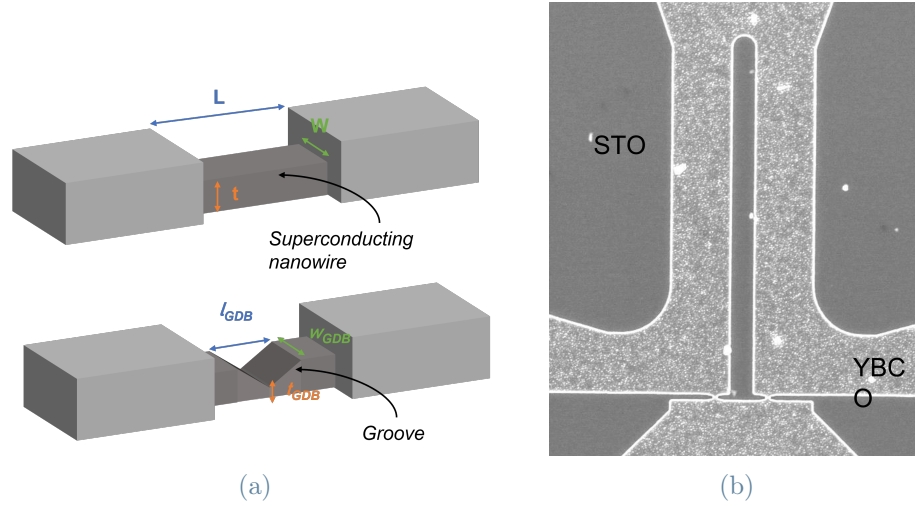


Figure 1.7: GDB-based SQUID: a) Nanowire and Groove Dayem Bridge weak links schematic comparison. b) SEM image of a SQUID, including hairpin loop

In order to overcome the limitations posed by DB-based devices, a new type of nanobridge has been developed: the GDB. It is substantially a bare nanowire in the middle of which it has been etched a groove, with the result of increasing the geometrical constrictions of the SC in that area. This allows for an enhancement of the electrical properties, otherwise impossible with simple DB-based SQUIDs. What happens, indeed, is that after the fabrication, the thickness of the pristine YBCO inside the groove is reduced to t_{GDB} , whose value depends on the etching rate. The groove acts on its own as a weak link, by reducing locally the superconducting properties of the nanowire and, as a consequence, the effective length and width to be considered are the ones of the groove. With respect to the DB-based weak link, it was found that the GDB is more akin in behavior to a *variable thickness bridge* [50, 51], where a central section of the structure has reduced geometrical dimensions. Moreover, it is important to consider the reduction to the superconducting properties due to the damage to the thin film done during the etching of the YBCO inside the gap. Therefore, the GDBs electrical properties are expected to depend strongly on the groove thickness and length l_{GDB} , which are both determined by the etching mask design.

For optimized GDB-based weak link, evaluated at 77 K, it was found a reduction in the critical current I_c of a factor up to 40 times lower than a bare nanowire with similar width [52]. However, we are not able to use the same parameters to evaluate their performances, since their Current-Voltage characteristic (IVc) is more similar to the one seen in the RSJ

model: for a bias slightly above the critical current, we find indeed a trend closer to the one obtainable with FIB-fabricated JJs and, therefore, more indicative of a SNS type of junction with respect to SS'S, with all probability due to the damage to the superconductivity properties conducted while etching. This similarity in behavior is also mostly reflected in the differential resistance $\delta V/\delta I$ curve, with the exception that, for a GDB, the resistance won't converge to a constant value for high bias. Therefore, the comparison to be done in order to understand the performances of such devices needs to be based on RSJ model figures of merit, as for example the characteristic voltage, $I_c R_N$. Higher values of $I_c R_N$ will be usually associated to better performing devices, where R_N is selected to be the $\delta V/\delta I$ value in the voltage range 100-200 μm . A GDB good value for this figure of merit was found to be in the range of 200-550 μV [26], for measurements conducted at 77 K. Still slightly lower than GB-based JJs, whose best characteristic voltages were found in the range of 800-1200 μm [39, 40], but where we need to consider that GB-based JJ are usually SIS JJs and not SNS. Nevertheless, GDB were shown already to be able to perform to a level comparable to the state-of-art GB JJs.

SQUID Magnetometers

SQUIDS have a broad range of technological applications in several science fields, such as sensors in biomagnetism, nondestructive evaluations, geophysics, as susceptometers, voltmeters, scanning SQUID microscopes, nuclear magnetic resonance, etc. However, one the most relevant ones, in particular when speaking of the magnetic-field sensing, is oriented to multichannel magnetoencephalography (MEG) measurements, in the biomagnetism field [53]. In recent years, indeed, SQUIDS have been used to detect several magnetic fields from the human body, starting from the very first measurement of magnetic signals from an heart, by Cohen *et al* [54] in 1970.

While initially those measurements revolved only around magnetocardiography (MCG) and MEG, later on the topic of study managed to extend to, for example, lung, intestine, fetus and spine. All of these research areas would benefit greatly from an improvement in performances of SQUIDS, justifying in this way the interest in obtaining more performing weak links which, in this case thesis, are the GDBs. However, particularly referring to MEG-aimed sensors, other requirements need to be accounted for, while fabricating and characterizing the devices.

Working principle of HTS-based SQUID magnetometers

Standard SQUIDS are extremely sensitive magnetic flux sensors, but due to the fact that

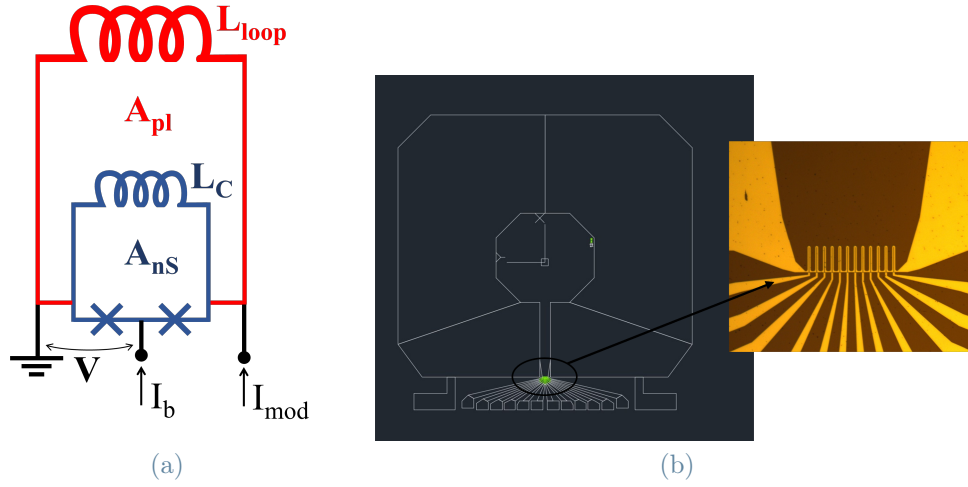


Figure 1.8: Magnetometer circuitual scheme on the left ((a), adapted from [26]) and EBL mask on the right, with a close-in picture of the SQUID series, taken from a sample during fabrication

they have a small effective area (A_{eff}), the magnetic field sensitivity is strongly limited. The effective area of a SQUID can be defined by Φ/B_a , where Φ is the magnetic flux through the SQUID loop and B_a is the externally applied field. This small value for A_{eff} needs to be increased in order to convert the nanoSQUID into an efficient magnetometer for, ad example, biomedical applications such as magnetoencephalography.

There are multiple solutions that can be implemented in the nanoSQUIDs, in order to fabricate SQUID-based magnetometers. The one that was chosen for this thesis work is the in-plane galvanically coupled pick-up loop. In this solution, several single SQUIDs are placed in series and coupled to the same pick-up loop (in the figure case, we have a series of 12 SQUIDs, but they can be up to 48 in total). The devices are characterized separately and the one with the best performance is chosen and used for the magnetometer application. Pictures of a SQUID magnetometer implementation, together with a schematics of the circuit, are presented in Fig 1.8.

The working principle of the SQUID-based magnetometer is the following: an applied external field B_a going through the pick-up loop leads to a screening current to be generated in it, $I_S = B_a/L_{loop}$. Due to the galvanic coupling, the current flowing in the pick up loop, flows in the hairpin loop as well. Here, I_S generates a phase difference between the weak links equivalent to $\Delta\Phi \propto I_S L_C 2\pi/\Phi_0$, where L_C is the coupling inductance between pick-up and the SQUID's one, i.e. the hairpin loop inductance, $L_{hairpin}$. This phase difference induces a modulation of the SQUID critical current.

The galvanic coupling between the pick-up loop and the hairpin one results in a total

effective area of the SQUID equal to [55]:

$$A_{eff} = A_{nS} + A_{pl} \frac{L_C}{L_{loop}}$$

where A_{nS} and A_{pl} are the effective areas of the bare nanoSQUID and of the pick-up loop, respectively. L_{loop} is the inductance of only the pick-up loop and it is dominated by its geometric component, due to the large linewidth of the loop.

From this relation we can now understand the differences in geometry of a SQUID magnetometer, with respect to a flux-sensing SQUID: in order to increase A_{eff} , it is important to increase the coupling, done by increasing L_C , which of course can be achieved with a larger value for L_{SQ} , inductance of the SQUID. This is the reason why for this application $l_{hairpin}$ is increased from $8\mu m$ to $l_{hairpin} = 49\mu m$. However, increasing L_{SQ} results in worse values for β_L , which therefore, ends up partially suppressing the current modulations of the SQUID. As a consequence of that, an optimal value for L_C needs to be found, coming from a compromise between the SQUID performances and the coupling requirements to obtain a good magnetometer.

Moreover, the dimension of the substrate on which is nanostructured the magnetometer limit A_{pl} value: in the case of this work, $10 \times 10 \text{ mm}^2$ STO substrates were used, leading to a maximum size for the pick-up loop outer dimensions of 8.7 mm x 9 mm with a linewidth of circa 3 mm.

2 | GDB-based SQUIDs fabrication process

In the following are reported and discussed the fabrication steps that were used in the course of this thesis to obtain GDB nanostructures on a YBCO thin film. While the process that will be presented is specific to this type of nanostructure, the bulk of it is derived from the one previously optimized for simple YBCO nanowires.

First of all, the growth and characterization of the superconducting material will be presented and the work done to optimize it discussed. The nanostructures fabrication will be then talked about in detail, with the last part of the chapter reserved to consider the aspects of the process that have been most challenging during this thesis work and have been possibly improved.

2.1. Growth and characterization of YBCO thin films

YBCO thin film growth is a very complicated process, as a consequence of the fact that many of this compound properties depend strongly on the stoichiometry that is obtained during deposition. In particular the level of oxygen doping has a determining impact on the outcome of the electrical properties of the material, while an overall homogeneity and micro-scale smoothness of YBCO thin films are also required in order to get reliable transport properties at the nanoscale.

These characteristics depend of course on the deposition technique that is employed for the growth of the YBCO thin film and on the deposition conditions. High quality thin films have been fabricated during the years by various methods such as rf magnetron sputtering, high-pressure dc sputtering, thermal co-evaporation, chemical vapor deposition and pulsed laser deposition (PLD). Among these techniques, we have chosen PLD, which however, together with high-pressure dc sputtering, is considered one of the most performing ones [8].

2.1.1. YBCO deposition and optimization of process

The deposition of YBCO thin films has been done through Pulsed Laser Deposition (PLD) and the quality of its results is strongly determined by the thermodynamic conditions at which it was conducted, the substrate chosen and the thickness desired.



Figure 2.1: Photograph of a STO substrate in the PLD chamber for YBCO deposition

With regards to the working principle of this technique: a pulsed high-energetic laser beam is focused on a target of YBCO, these pulses result in ablation of some of the target material, which will then deposit on the substrate placed directly above it. The mixture of atoms, molecules, ions and clusters that arises from the target forms a so-called *plasma plume*, due to its characteristic shape, as it can be seen in Fig.(2.1) reported above. The plasma plume then emerges from the target and condensates on the heated substrate in front of it results in the growing of the thin film with each laser pulse.

Depending on the substrate chosen and on the purpose of the YBCO thin film, various parameters of deposition need to be optimized in order to get to the optimal growth conditions.

We have grown YBCO either on MgO(100) or on STO(001) substrates. While MgO is the preferred substrate for the investigation of the base physics of YBCO, and for the growth of untwinned thin films subject to a compressive strain [56], STO is a much more suitable substrate when one aims at maximizing the critical temperature T_c , as in this thesis work.

Indeed, on STO T_c up to 90-91 K can be achieved, which is fundamental for the growth of nanostructures such as GDB, due to the fact that the superconductivity of the weak links will be slightly suppressed, due to the loss of oxygen during fabrication. If the weak links have too low of a doping, they may be resistive around 80 K, our working temperature, and not function any longer as a SS'S JJ.

Substrate dimensions	T_{dep}	p_{dep}	d_{t-s}	E_{laser}	p_{post}	pulses	t_{YBCO}
	K	$mbar$	mm	mJ	$mbar$	-	nm
STO(001) 5X5	755	1.0	55	58	1.0	900	50
	755	1.0	55	58	1.0	1200	70
STO(001) 10X10	795	0.7	55	57	866	1200	70

Table 2.1: Summary of deposition condition for YBCO on STO substrate. The table shows the optimized parameters for deposition of samples of 50-70 nm of thickness on 5x5 mm² chips and 70 nm thick on 10x10 mm² chips. The latter is usually oriented to SQUID magnetometer fabrication.

As a result, all the devices in this work have been fabricated on STO substrate.

The substrate is prepared for deposition through a simple cleaning in Acetone or IPA and ultrasounds, followed by a short pre-annealing of around an hour at the deposition temperature inside the deposition chamber.

With regards then to the growth of YBCO films on STO, in the following table are reported the parameters chosen for an optimized deposition process:

All these parameters, as well as manipulator position with respect to the axis of the chamber, the cooling rate, the laser fluence (2 J/cm²) and the laser repetition rate (6 Hz), concur to the determination of the properties of the thin film that will be grown.

In particular, parameters such as the oxygen pressure (p_{dep}), substrate temperature (T_{dep}), relative position of target and substrate (d_{t-s}) and fluence, pulse energy and repetition rate of the laser all contribute to control the size and shape of the plume, which then correlates to the surface kinetics of the deposited atoms.

On the other end, the value of the pressure for the oxygen in the chamber after deposition (post annealing pressure, p_{post}) and the cooling rate will be responsible for the resulting doping level of the YBCO thin film, as they do regulate the oxygen flow in the chamber, and therefore the diffusion of it into the film during its cool down from T_{dep} to ambient temperature after deposition.

The deposition parameters have been chosen in order to get the best possible compromise between a smooth, homogeneous surface and a sufficiently high critical temperature T_c of the YBCO film, both fundamental for nanofabrication. In particular, an increase of T_{dep} leads to a higher superconducting critical temperature, at the expense however of the surface morphology; a reduced T_{dep} instead, leads to a smoother surface at the expense of the desired doping of the material, therefore of the critical temperature and sharpness of the superconducting transition. Considering that our goal for the growth of this films is to

obtain nanostructures, of which the electrical and transport properties strongly depend on their superconductivity behavior, we aimed for a slightly overdoped YBCO film ($p > 0.16$) and found the right compromise for T_{dep} at around 755°C for $5 \times 5 \text{ mm}^2$ and 795°C for $10 \times 10 \text{ mm}^2$ thin films, as reported in the table.

The growth conditions have been optimized for both 50 nm thick YBCO films and 70 nm, which, as a matter of fact, differ only in the number of pulses needed per deposition. They are however both mentioned due to the vast difference in the electrical properties stability obtained for the nanostructures on $5 \times 5 \text{ mm}^2$ samples, in particular with respect to GDB fabrication. A distinction has been made also between $5 \times 5 \text{ mm}^2$ and $10 \times 10 \text{ mm}^2$ YBCO films in Tab (2.1), as the two depositions have to differ in temperature of deposition and position of the substrate with respect to the plume.

As a last note in this section, I would like to mention that, although the set of values for deposition parameters that has been presented is an optimized one, it is not the only optimized configuration for the growth of this material that will result in a smooth surface and high critical temperature. There are, as a matter of fact, several possible sets of values for those same parameters that will result in a "good compromise" for the thin film deposition.

2.1.2. Characterization of YBCO surface and properties

In this section, the results of the morphological and electrical characterization of the YBCO films deposited on STO(001) through PLD will be presented. The substrate chosen is, as mentioned, a (001) oriented STO, with a nominal vicinal angle of $\alpha_V = 1.0^\circ$, whose cut is directed along the (010) direction.

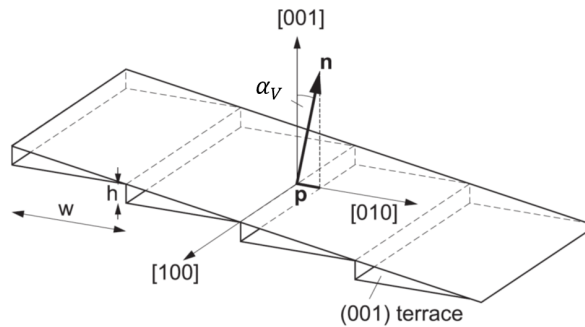
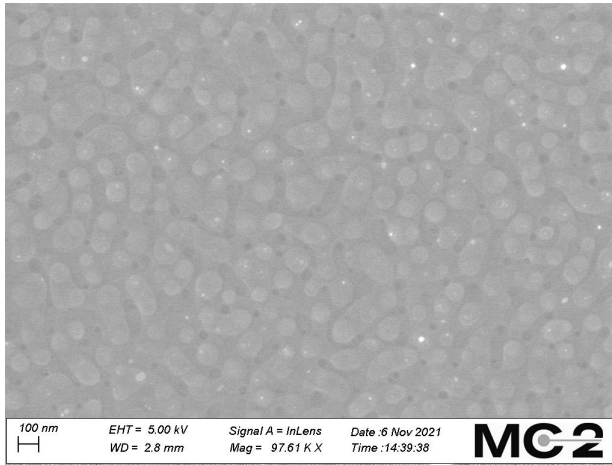


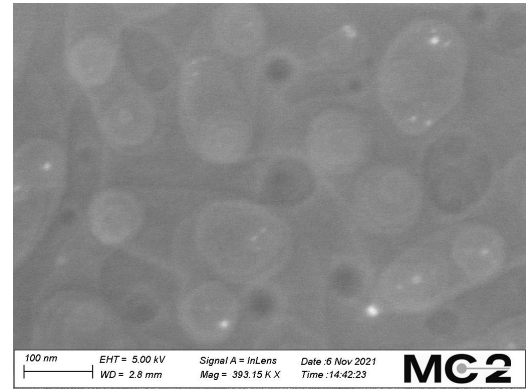
Figure 2.2: STO surface with 001 terraces. Adapted from [8]

As a consequence, the surface of STO substrates exhibits a periodic sequence of steps as shown in Fig.2.2.

The surface is constituted by (001) terraces, of height h_T , and whose width w_T decreases when α_V is increased. When a YBCO thin film is grown on top of these terraces, a strain (different from the one applied by an MgO substrate) occurs at the interface between the materials, due to the small lattice mismatch between the cubic STO substrate ($a = 3.905 \text{ \AA}$) and the unit cell of the YBCO film, which transforms in post-annealing from tetragonal to orthorhombic. Since STO strain is strongly anisotropic, it prefers to shrink perpendicularly to the step edges, where atoms are under coordinated, and, as a consequence, its surface along the terraces direction is distorted into a rectangular lattice. This distortion will as a consequence influence the growth of the twinning domains of YBCO thin films: the b-axis of YBCO unit cell will tend to align along the step edges, where STO lattice parameter results longer. With this condition of substrate and the optimised parameters for deposition of YBCO mentioned in the section before, we obtained a YBCO surface pattern as shown in Fig. 2.3



(a) SEM image. Magnification 100K



(b) SEM image close-in, for better visualization of pattern. Magnification around 400K

Figure 2.3: SEM images of YBCO surface, optimized sample. Not oriented with respect to a and b axis directions

Thin film morphology has been studied through the use of Scanning Electron Microscopy (SEM), at low levels of energy for the electron gun and small distances from the surface (few mm), with several magnitudes, in order to have a complete view of YBCO surface while avoiding as much as possible charging effects of the surface. As it can be easily noticed, the film presents a very smooth surface with few small holes, clearly characterized by c-axis spirals (islands), indicating a 3D type of growth of YBCO over STO.

Transport properties: $R(T)$

Along with morphology properties of YBCO, transport properties of the thin film have been studied, principally through resistance vs temperature $R(T)$ measurements (see Fig. 2.4).

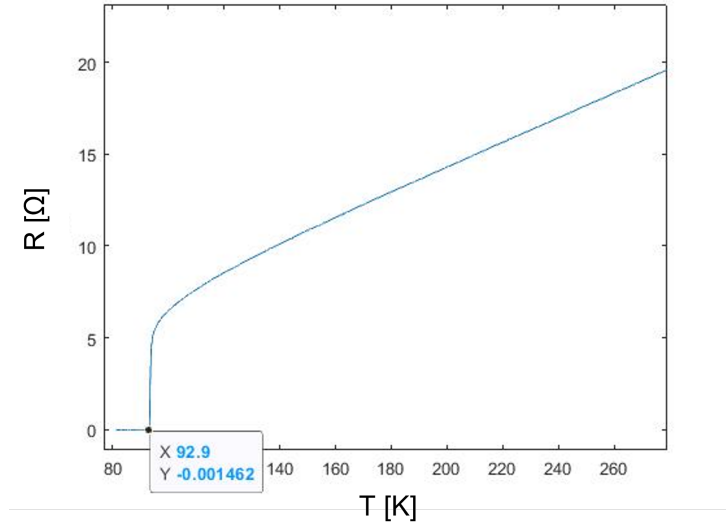


Figure 2.4: Resistance with respect to temperature curve for an optimized YBCO thin film deposition. In this specific case, it is presented one of the sharpest and highest critical temperature transitions obtained through optimization of YBCO deposition during this thesis work. Transition starts at $T > 93$ K and concludes around $T = 92.9$ K

The measurement is conducted by applying a bias current between two sets of points on the YBCO thin film surface and retrieving from the measured voltage drop between them the resistance of the thin film. Resistance is plotted with respect to temperature, while the sample is lowered in liquid nitrogen and left reaching the equilibrium at 80 K. The critical temperature T_c is defined in this work at the end of the superconducting transition and is, in the case presented, around 93 K, which is, admittedly, quite high with respect to what is actually needed to build nanostructures with it. This possibly signifies that the thin films produced with this recipe were not much overdoped, but closer instead to be optimally doped (see Fig. 1.2 for the position of the superconducting dome peak with respect to oxygen doping). We can then conclude the recipe is adequate enough, since it appears to produce optimally doped YBCO thin film.

The homogeneity of the thin film can instead be derived by the sharpness of the transition, of possibly even less than 1 K.

2.2. Fabrication

In this section, the fabrication steps for the Groove Dayem Bridges will be presented in detail. GDBs, as high quality YBCO weak links for SQUID applications, are a relatively new type of nanostructure and their fabrication was presented for the first time in [26]. A GDB fabrication is obtained by modification of a bare nanowires process (DB), where steps are added in order to reduce the height of the nanostructure around its middle, creating thus a constriction, groove, inside the weak link. This will give enhanced electrical properties with respect to bare nanowires, consenting to overcome most of their limitation in critical current I_c and inductance L_{SQ} , which usually put a lower limit to β_L value and, therefore an upper one to the performances obtainable from nanowire-based SQUIDs.

In the following, the focus will be specifically on the groove fabrication, since it represents the most complex and optimizable part of the process for the resulting electrical properties. The fabrication has been conducted in the Microtechnology and Nanoscience Laboratory (MC2) at Chalmers University of Technology, Gothenborg, Sweden.

2.2.1. GDB nanopatterning process



Figure 2.5: YBCO deposited on STO substrate with the PLD system.

Right after the deposition of the superconducting material, a thin layer of gold (around 40 nm-50 nm) is sputtered on top of a portion of it (through the use of a simple mask). The gold layer will function as the contact point for the measurements after fabrication and will be necessary in order to have good low-noise results. Fabrication in itself will however still be feasible (achievable) even without it.

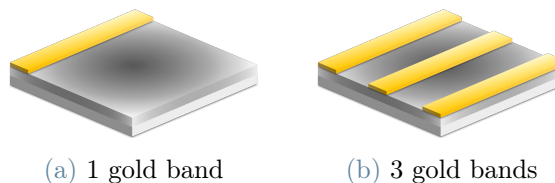


Figure 2.6: Sputtering of gold over YBCO with Metal sputter for bonding pads

Then a carbon layer is used as a protective mask for the YBCO. Once placed, the oxygen doping level and the overall quality of the material will be protected from the environment until the layer is removed. Carbon is chosen as a protective material due to its robustness to Ar^+ ion milling, since it takes much longer to etch than YBCO, and it is easily removed with a step of oxygen plasma etching without risking any damage to the structures patterned underneath. Carbon is deposited once again through pulsed laser deposition and the outcome of the process is of fundamental relevance for the final result of our modified nanostructures [57].

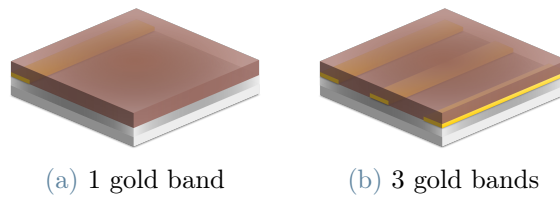


Figure 2.7: Deposition of Carbon over YBCO with PLD. It will act as a protection for the superconductor surface during fabrication

A double layer of resist is spun on top of it in preparation to the patterning of the nanostructures. The two blends are negative photo-resists, MMA(8.5)MAA EL4 and AR-P 6200.13 1:1 respectively, spinned 6000 rounds per minute and for 90 seconds and will result in a final added thickness of 120 nm. The resists are layered in this order so that, when exposed to the electron beam in the following step of lithography, they will have a slightly different exposure result. The lower resist, the first layered, will indeed result slightly more exposed than the upper one. This ensure a better result during the subsequent lift-off step.

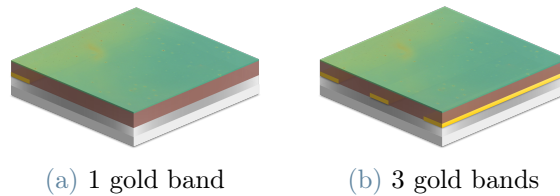


Figure 2.8: Resist deposition. Color in the picture is taken from a microscopy photo of this point of process during fabrication.

The patterning of the nanostructures is done through electron beam lithography. A mask for the sample is created in AutoCAD. The exposure consists of two exposition steps, already proximity corrected for our material and substrate material, which are a high

current step, for the exposition of the wider parts of the structures as the electrodes or pick up loop, and a low current step. This latter step is needed for the exposition of the smallest features of our devices, first and foremost the groove Dayem bridges, for which the lower resolution limit of the machine, paired with the type of resist chosen, sets a lower limit in length and an upper limit in width. Due to this, the groove in the nanowire cannot be smaller than 30 in length and 100 in width.

Development of the resists follows exposure. For the development, we have used two developers, o-xylene UN1307 first and MIBK:IPA 1:3 second, one per resist and each for an immersion time of circa 35 seconds. Being the resists positive photoresists, the exposed parts will be the ones to be removed.

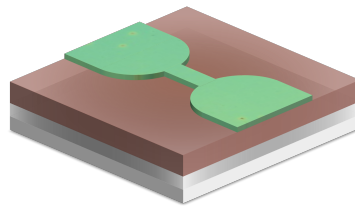


Figure 2.9: Development of the EBL mask after exposure. The gaps for GDBs are at this moment patterned.

A 12 nm layer of chromium Cr is evaporated on top of the developed double layer resists and it will act as a protective mask for the carbon underneath the patterned structures.

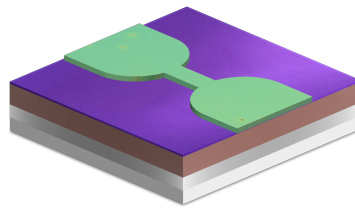


Figure 2.10: Evaporation of Chrome over the developed sections.

Indeed, following evaporation, all the remaining resist is removed with a step of lift off, as in 2.11. For this purpose, we submerge the sample in remover 1165, heated at 75°C, for 8 minutes, followed by circa 1 minute of low power ultrasound. Any left-overs are then removed with a cleaning in IPA and a second low power ultra-sound step.

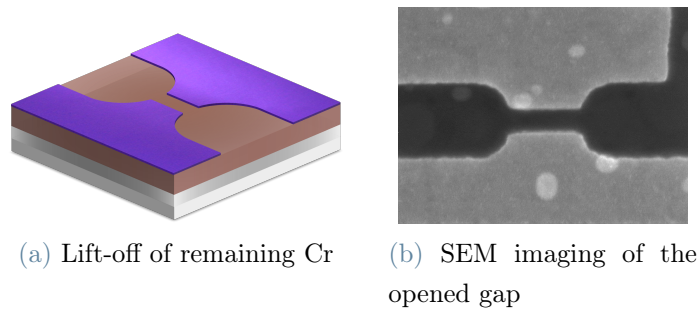


Figure 2.11: Lift-off and SEM images of an exposed mask and developed mask.

This series of steps is also crucial for the GDB nanostructures fabrication: indeed, the dosage of the exposition as well as the times for development and lift off steps must be carefully optimized in order for the pattern to be well transferred to the carbon underneath and the gaps in the nanowires to be well defined and of the right dimensions. At this point in the fabrication, a step of SEM imaging is added to check the lithography 2.11.

The mask is now transferred to the carbon layer through a step of reactive oxygen plasma etching. As a matter of fact, this process does not interact with the chrome mask nor, within certain limits of power and pressure, it damages the YBCO film laying underneath. The process is done in oxygen environment, at 100 mTorr of pressure, at power 50 Watt and it is kept on for at least 22 minutes, in order to be sure to etch completely through the carbon layer.

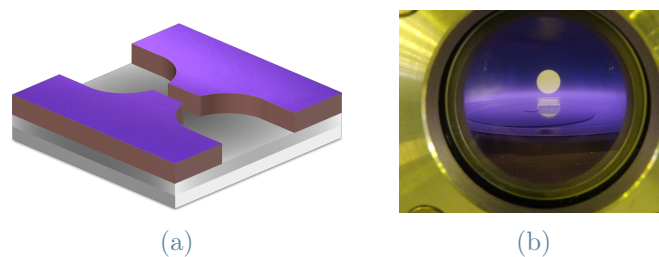


Figure 2.12: Plasma etching stage for removal of unprotected C: schematics and a photo of the process in progress

Once the mask is impressed on the carbon, the actual nanostructures can be etched into YBCO with a step of ion beam milling. The argon ions will remove the protective layer of chrome, etch through the YBCO film and into a fraction of the carbon protective mask. This process outcome revolves around several parameters that must be tuned together in order to obtain the best conditions for defining the nanostructures. With respect to all

the other weak links fabrications, in the GDB case the ion milling acquires a much more prominent role and the optimization of this step is not straightforward.

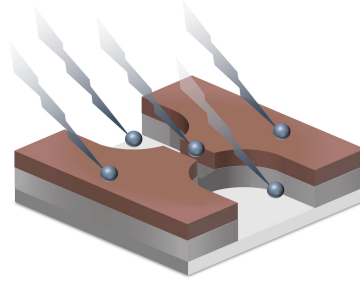


Figure 2.13: Ion milling etching of GDB into exposed YBCO. Although C is resistant to this type of etching, 20-25 nm are still lost from the mask at the end of it.

Lastly, we etch all the remaining carbon with a second step of plasma etching.

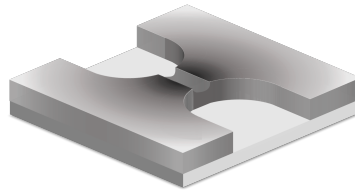


Figure 2.14: Removal of all remaining C mask over YBCO

Fabrication of GDB-SQUID is at this point concluded and sample is brought out of the clean-room for characterization of its resulting electrical and transport properties. It is worth to mention that profile measurements are done on the sample throughout all fabrication to check the step height and verify that the etching steps have reached conclusion before proceeding with fabrication's next step.

2.3. Carbon mask deposition

Carbon is deposited on the YBCO through pulsed laser deposition and, while parameters such as chamber deposition pressure (3.4×10^{-4} mbar), frequency of pulses (10 Hz) and distance between target and carbon sample (5 cm) are established based on the optimal condition for deposition, several others such as laser energy and deposition time need to be tuned in order to obtain the required conditions for the protective mask.

Laser energy: Considering to keep a fixed laser spot size at 4mm^2 , a good way to control the carbon layer hardness is to tune the laser energy. As what happens for YBCO deposition, the laser energy is correlated to the surface kinetics of the deposited carbon.

It was found that, for higher energy the film of carbon atoms will dispose to grow a much harder thin film surface, with respect to what happens with a low energy pulse, where the carbon film obtained will be much softer. The energy to be chosen depends therefore on the requirements for the carbon layer, which are that, while it needs to be a hard enough mask to protect the surface, etching through with reactive plasma etching must still be possible. Moreover, a too hard layer of carbon would likely have adhesion issues to the underneath layer during fabrication and much more easily break. On the other end, a very thin soft layer of carbon (low energy, around 70/80 mJ) does allow for a much more reliable adhesion of the mask to the superconducting surface, and while it could be speculated that it may introduce unknown effects in later stages of the fabrication, by for example reacting differently during etching stages, we have not observed any significant differences with comparable samples protected with a much harder carbon mask. In conclusion, for the vast majority of the samples fabricated during this thesis, we chose to apply three layers of carbon, with an increase of the laser energy of more or less 20 mJ for each layer (the values being around 70 mJ, 90 mJ and 110 mJ).

Deposition time: Tuning of deposition time affects the thickness of the carbon mask, which, as it is later shown, was found to be the most reliable for GDB fabrication when around 100 nm high, corresponding to 30s at 70 mJ, 60s at 90 mJ and 90s at 110 mJ. At such height the mask is able to work both as an effective protection during overall fabrication and as the right step with respect to the YBCO, for when the grooves are etched in the ion milling stage.

The carbon mask assumes, indeed, both the role of a protective layer and of a shadow-casting one while the superconductive material is etched into by the Ar^+ ions: its height does determine, together with the geometrical characteristics of the weak links and the ion milling parameters, how fast the etching is conducted and what portion of the opened gap area will be directly affected. Its direct correlation with the outcome of the ion milling step is why the carbon deposition is such a fundamental step of the fabrication, especially for GDB nanostructures. It was found that changing the height of the mask leads to dramatically different results in the transport and electrical properties of the resulting nanostructures, even to the point of rendering them completely unreliable, as it will be shown at the end of next chapter.

2.4. Ion Milling process: etching of the mask

As mentioned previously, the Ion Beam Etching (IBE) step has a very relevant role in the fabrication of GDBs. This is, in fact, the stage in which the grooves are etched into the

superconducting material. Essentially, the sample, still mostly covered with the carbon mask, is mounted onto a platen and transferred into an ultra-high-vacuum chamber, where it undergoes physical etching by an Argon ion beam. The ion beam arrives on the sample surface at an angle, α_{IBE} , which it can be selected between 5° and 90° , where $\alpha_{IBE} = 5^\circ$ results in an almost vertical etching. While the sample is etched, a rotation of 5 rounds per minute of the platen is active, to ensure that the etching is uniformly done from all directions. The time for the etching is decided by observing the behaviour of the atoms per counts curve of a two to three specific elements, which are known to be easily detected by the secondary ion mass spectrometer (SIMS), paired with an electron multiplier, during etching of the YBCO film. In our case, atoms per counts of Strontium, Barium and Yttrium were selected in order to follow the etching process. In the following figure is an example of Strontium and Barium detection curves of an ion milling process, imaged with the SIMS software:

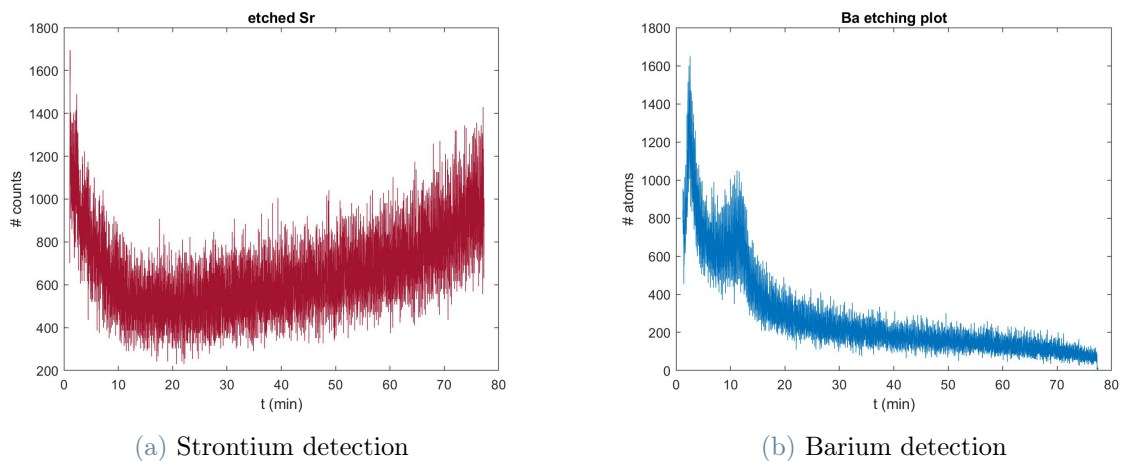


Figure 2.15: SIMS linear graphs related to IBE of YBCO. Sr on the left, rising when substrate starts to be exposed. Ba on the right, to monitor YBCO etching

In setting up this process, many parameters can be modified in order to etch differently and, thus, to obtain different electrical or geometrical results on the weak links and, for this reason, tuning them is fundamental. For example, small changes in the current of the ion beam or in the neutralizer will result in drastic changes in the speed of the etching process and therefore in the time needed for the etching, while other parameter like the etching angle or He cooling will imply much more controlled changes, which can be still very determining for fine tuning the electrical properties of these nanostructure's properties.

3 | Characterization of SQUID properties

Following the fabrication introduced in the previous chapter, in the current one the electrical properties of GDBs will be presented, with respect to the results obtained in previous and current works. The electrical transport properties are shown to be strongly dependent on the geometry of the weak link, therefore on the parameters chosen for the etching mask.

The aim is to stretch the already found advantages of GDBs over bare nanowires to its most, by optimizing their performances at HTS working temperatures, namely around $T = 77$ K, where N_2 liquefies.

Beside the width w_{GDB} and the length l_{GDB} of the groove, which were already found to have an important role in determining the weak link properties [26], this mainly implies the optimization of the etching time and the conditions of etching. In fact, we found that the thickness of the groove t_{GDB} is strongly related to the etching time and the height of the carbon mask, while the quality of the YBCO in the groove depends on the parameters that have been chosen for the etching, such as the angle of etching, α_{IBE} . The quality of the YBCO in the grooved area, indeed, determines which model represents best the final device: RSJ, and therefore SNS, when the material in the groove is quite damaged and has partially suppressed superconducting properties, or SS'S, when the GDB appears to be more closely related to a nanowire weak link, which usually occurs when the damage conducted on the weak link is not sufficient to reduce its superconducting properties close to or below the temperature of liquid N_2 . As it will be shown in the last sections of this chapter, this implies that fabrication parameters such as the ones of the ion milling play a fundamental role in the optimization of these devices.

In order to evaluate the performances of our GDB-based SQUIDs, we have centered our investigation of the transport properties on the differential resistance δR , the critical current I_c and, lastly, the ΔV of the SQUID. While the kinetic inductance of the groove, L_k , is a relevant parameter as well, in this contest it is mostly connected to the quality of

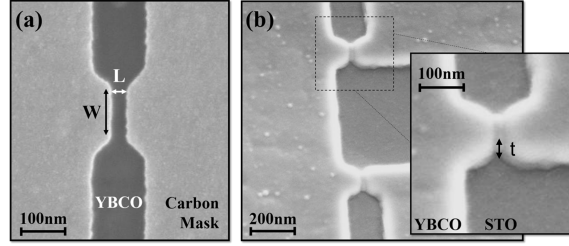


Figure 3.1: SEM images of a GDB. On the left, a SEM of the gap that has just been opened in the C mask, with length and width shown. On the right, a fabricated GDB, with a close-in on the groove. Adapted from [26]

the YBCO thin film and to the thickness chosen for it. Simply speaking then, we consider a GDB-based SQUID to be an optimal one, if it presents a high differential resistance δR (circa 10Ω at the SQUID working point), a relatively low characteristic current I_c (under $200 \mu A$), all the while maintaining a low kinetic inductance L_{kin} (around $20 pH$ for a 50 nm film, $40 pH$ for a 70 nm one). For the conditions presented, we were able to produce GDB-based SQUIDs, with voltage modulations as high as $15 \mu V$, which, while this is not yet comparable with the state-of-art given by GB-based SQUIDs, it is a good starting point from which one can further improve performances of the weak links and get to competitive results.

3.1. GDB-based SQUIDs: characterization of electronic properties

Starting the discussion on optimization of GDB-based from the geometrical parameters of the nanogap in the weak link, it is first of all important to consider the outer limits that the fabrication poses to our choices for l_{GDB} and w_{GDB} (in Fig.3.1 as L and W, respectively).

There are, indeed, minimal feature sizes that can be achieved with electron beam lithography (EBL) that restrict our investigation. It is in fact challenging to expose nanogaps with length $l_{GDB} \leq 20 \text{ nm}$.

The exposed mask is not reproducible for such small length and might result in undesired connections between the mask on the sides of the nanogap. This sets a lower limit for the groove length at $l_{GDB,min} \simeq 30 \text{ nm}$. Fortunately, as it will be shown later, in order to achieve a critical current I_c low enough for our purposes, the nanogap length needs to be $l_{GDB,min} \geq 30 \text{ nm}$. On the other hand, EBL introduces also an higher limit for the width

of the groove w_{GDB} , since exposure becomes equally challenging for wider nanogaps, if maintained same length l_{GDB} , once again due the higher possibility of not having a proper opening of the mask in those grooves. Not only it would be challenging to achieve, but we found no substantial improvement in the electrical properties, such as a decrease in I_c , for $w_{GDB} > 300nm$, even for bigger l_{GDB} lengths. Therefore, we restricted our investigation to $w_{GDB} \leq 300nm$.

On the other hand, w_{GDB} has a lower bound as well, given by the etching process done with Ar^+ ion milling. In fact, for gaps with $w_{GDB} \leq 150nm$ we found that the process results in non-reproducible outcomes in terms of I_c value, thus not being suitable for technological applications. Moreover, differently from what happens with nanowires, it is convenient for us that w is as wide as possible, since it lowers L_{kin} of the weak link and a larger w is not as detrimental to the electrical properties as an higher parasitic inductance. This is due to the fact that, while it should intuitively increase I_c and therefore worsen the β_L value, for GDB-based SQUIDS, I_c is much more strongly related to t_{GDB} value, which is instead affected inversely by the increased width.

For all these reasons, we choose as an optimal range for the width $200nm < w_{GDB} < 300nm$. Moreover, we found that weak links electrical characteristics do not change substantially in this range for w , but are more effectively determined by our choices for l_{GDB} and resulting t_{GDB} .

On this note, optimization of l_{GDB} and t_{GDB} are much less straightforward. In fact, they are reciprocally dependent, in the sense that, a GDB with bigger l_{GDB} will lose its superconductivity and, therefore, become resistive if not enough superconductive material is present in the groove (t_{GDB} value is not high enough). On the other hand, if the material is not damaged enough or the groove is too shallow, the GDB will act exactly as DB and, therefore, not be able to produce detectable voltage modulations at 77 K.

Intentional damage inside the groove, however, can be relatively controlled during the ion milling step, as it will be shown later, and in this way, two optimal areas for the geometrical parameters were found, as it can be seen in the table 3.1. While the one at $l_{GDB} = 40 - 50nm$ was already reported in previous work [26], the other (at $l_{GDB} = 90 - 100nm$) was found by applying a "softer" etching step of the material. Not too different results were obtained by using either $w = 200nm$ or $w = 300nm$.

As it can be noticed from the IVCs of the two GDB-based SQUIDS brought as example, even though both were found to perform similarly in terms of voltage modulations ($12 \mu V$ and $15 \mu V$), differences in the shape can still be noticed. Indeed, while the IVC of the second GDB SQUID appears to have a shape more closely related to what one would

IVC and δR	l_{GDB} [μm]	w_{GDB} [μm]	I_c [μA]	R_N [Ω]	$I_c R_N$	ΔV [μV]
(a), (c)	50	200	50	10	500	12
(b), (d)	100	200	212	5	1060	15

Table 3.1: Summary of the electrical properties extracted from the data presented in Fig. 3.2 for optimized GDB SQUIDs, at $T= 77$ K

expect from RSJ type of JJ just above I_c , the first shows a more "rounded up" behavior, typical of what was found for DB SQUIDs. It is worth mentioning, however, that the resemblances stop when I_b is pushed much above I_c , since, instead of converging to a fixed value as shown in the introduction, it continues increasing. Nonetheless, for what concerns the IVCs, we may speculate that the second junction was somehow more damaged during the fabrication process and resembles more closely a SNS JJ, where instead the first shows a SS'S type of shape. However, the differences are minimal between the two cases presented and therefore more easily imputable to the specific device fabrication than to the etching mask characteristics.

To compare the electrical properties of the GDB-SQUIDs we have used, specifically to the GDB weak link, the characteristic voltage $I_c R_N$, and for the whole device the voltage modulations resulting from the current ones. Since R_N parameter cannot be obtained by saturation of the resistance at high current bias, we will approximate it with $\delta V/\delta I$ value in a voltage range of circa $100 \mu V$ just above the critical current, as was presented in the introduction and done already in previous work [26]. A summary of them is presented in the above table.

The GDBs we built during this work were able to give characteristic voltages in a very large range, mostly being in line with what was already obtained previously [26], and a maximum of $15 \mu V$ of modulations at 77 K. While this constitute a possibly promising result, it is worth to notice that the noise levels of these systems at operational temperatures are still too high for these performances to be satisfying in applications. We therefore worked on further pushing the geometrical parameters to their most performing limit, found to be at the verge between a SS'S JJ and a SNS one.

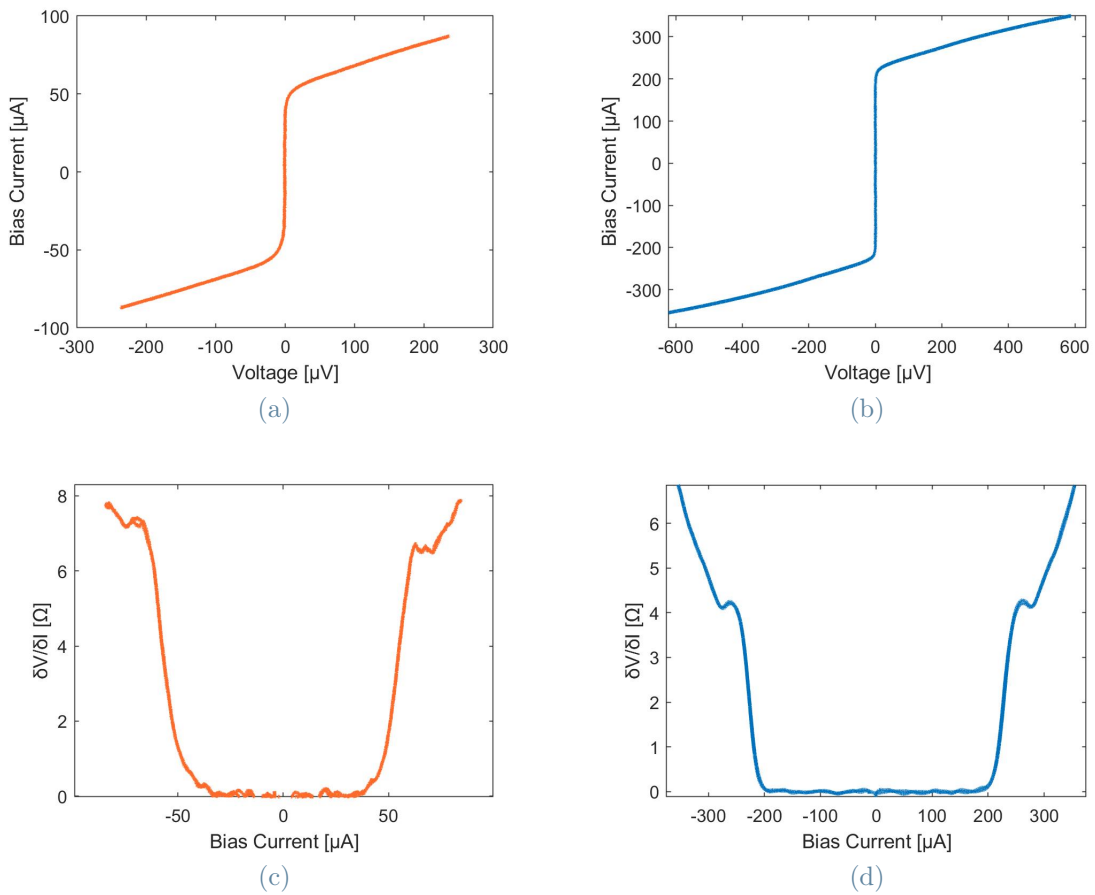
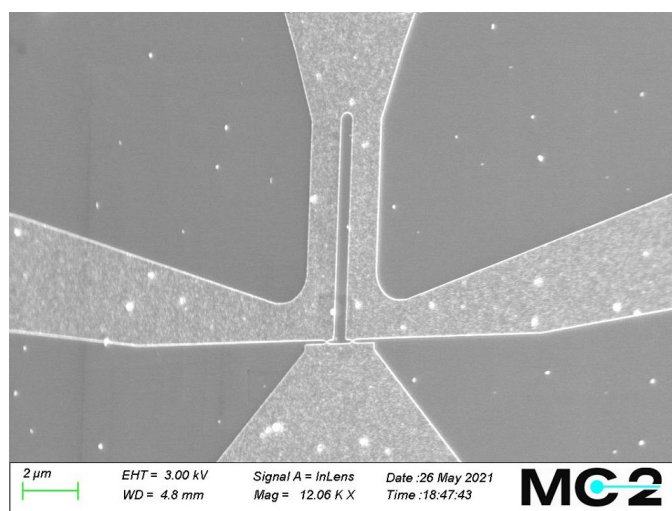


Figure 3.2: Current voltage characteristics and differential resistance of two GDBs built with different etching masks. (a)-(c): 50/200 gap; (b)-(d): 100/200 gap



(a)

Figure 3.3: Image taken with SEM of a measured SQUID.

Lastly, with regards to specifically the implementation of GDB as JJ for SQUIDs application, we must consider the contribution of inductance on the performances given by the hairpin loop $L_{hairpin}$. Since for a GDB SQUID, I_c and L_{kin} of the weak link are lower, we can implement larger SQUID loops while not compromising excessively the modulation depth of the device or worsening the magnetic flux noise, $S_{\Phi}^{1/2}$. Increasing the dimension of SQUID loop is pivotal for sensing applications of the device, as it will be discussed in ch. 5. A good value for $L_{hairpin}$ was found at 8 μm .

As a final note for this section, it will be briefly mentioned the relationship of electrical performances with respect to the working temperature of the system. In Fig. 3.4, c), is shown the voltage modulation depth at the working point of the SQUID as a function of the temperature T . This shows part of the complexity of physics of transport of a GDB. Indeed, while it was found that at very low T , the value of ΔV_{max} decreases rapidly, until it reaches a plateau for $T \geq 25\text{K}$, it then increases until a local maximum, found around $T \simeq 80\text{K}$, around the LN_2 temperature. At $T > 85\text{K}$, it then decreases until zero, in correspondence with the critical temperature of the GDBs. This shows the non-monotonic trend of ΔV , caused by a non-monotonic behavior of δR with temperature, while ΔI_c just decreases. This δR peculiar behaviour is typical of junctions that transition with temperature from SS'S to SNS [26], and it can be reasoned with by assuming that, due to unintentional damage during fabrication, different values of T_c have resulted along the weak link. However, the consequence of this ΔV behaviour is that the voltage modulations found at LHe temperature will be always much more evident than the ones at LN_2 . In Fig. 3.4, a) and b), it can be found an example of the result of measuring the same devices, first at 77 K and secondly at 4 K:

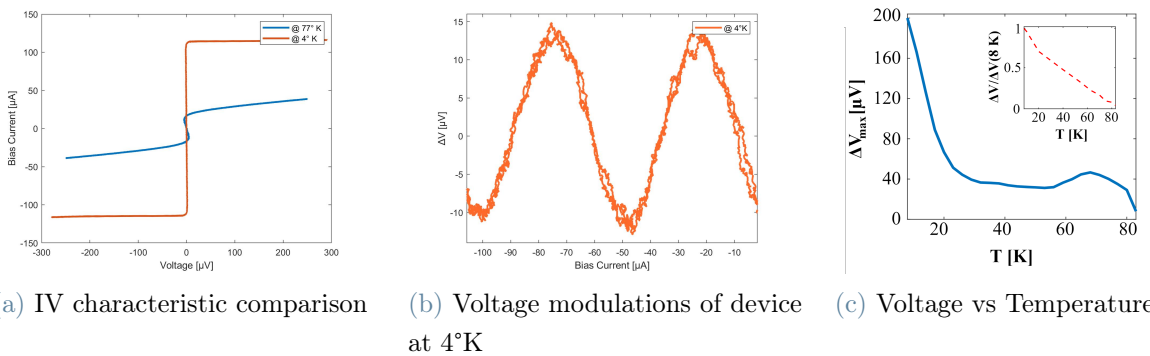


Figure 3.4: (a) and (b) show a comparison of a device IVC between 77 K (blue line) and 4 K (orange line) measurements. No detectable modulation was found at 77 K. Figure (c) describes the behavior of voltage with respect to temperature

3.2. Optimization of GDB-based SQUIDs

As it was underlined in the previous section, much of optimizing the performances of GDB SQUIDs depends on the groove height itself, t_{GDB} . In fact, together with the l_{GDB} , it is one of the parameters to which electrical results will be more sensitive to. However, it is also a very challenging parameter to control, since we are not able to directly preset it and we will need to rely on optimizing it indirectly. Several stages of the fabrication are involved in this process, but we have found to be the most critical ones the carbon deposition and the ion beam etching.

Another aspect of the problem that is important to consider when choosing a t_{GDB} for GDBs is reliability. In fact, while it may look as the most intuitive choice to reduce the height of the GDB as much as possible, in order to obtain the most dramatic change in superconductive properties along the wire, it usually concretizes in a more "aggressive" fabrication that ends up resulting in resistive GDBs. This is connected as well to the quality and the thickness of the YBCO thin film used: by using a not sufficiently optimized YBCO film, we have found that the electrical properties of the GDBs are not anymore behaving as expected due to the local non-homogeneity of the thin film. The same way GDBs built in a film too thin will be more susceptible to defects or unintentional damages during fabrication, resulting in this case as well in non-reliable results.

GDB-SQUIDs: role of the carbon mask

Carbon deposition is a step of fabrication that can be tuned by, mostly, laser energy and deposition time, as was explained at the end of ch.2. While the laser energy needs to be optimized in order to have an effective mask for the protection of pristine YBCO thin film, deposition time indirectly affects the height of the resulting GDBs, t_{GDB} . Indeed, as it can be seen from Fig.3.5, the carbon layer that was opened up in correspondence of the GDBs for etching, extends a "shadow" over them during the etching phase. This is due to the fact that, as was seen prior, the etching happens at an angle, therefore the amount of argon ions per unit time entering the gap depends on the height of the carbon mask.

The height of the mask needs then to be tuned to determine how rapidly the etching is going to proceed during the ion milling stage. We investigated the electrical properties of GDB SQUIDs, keeping all parameters fixed, except for the carbon mask, for which we chose to restrict the value for its height between 60 nm and 100 nm.

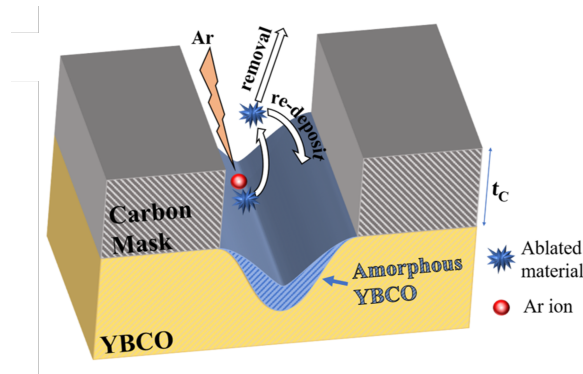
<i>CarbonHeightvsIVC</i>	Gap 1	Gap 2	Gap 3
60 nm	5 μm	RES	OC
78 nm	162 μm	OC	7 μm
85 nm	5 μm	RES	OC
105 nm	395 μm	91 μm	181 μm

Table 3.2: Table of averaged IV results with respect to carbon mask height and geometrical dimensions of the nanogap. This investigation has been conducted on YBCO films 50 nm thick.

The results of the investigation are summarized in table 3.2. From the wide changes in I_c found, we derive that reducing the carbon mask height below 100 nm, usually results in a strong increase in unreliability of the electrical properties of the resulting GDBs. In contrast, the IVCs for GDBs with similar geometrical dimensions, but carbon mask height above 100 nm, show once again stable I_c , with a variability of maximum around 15 %.

Therefore, while reducing the carbon mask height effectively reduces the I_c of the devices, it does so unpredictably and appears then to not be the correct way to approach the problem of the GDB height, t_{GDB} .

GDB-SQUIDs: role of the ion milling



(a)

Figure 3.5: GDB schematics for ion milling etching and redeposited material. Adapted from [52].

The ion milling etching step is, once fixed the carbon height, the step in which the shape of GDB and t_{GDB} are determined. While too many parameters concur to the final exact shape of the groove, the thickness of it is directly correlated to current intensity of Ar^+ ,

I_{Ar} , the etching time t_{IBE} , the etching angle α_{IBE} and the temperature of environment T .

To minimize damages and oxygen-out-diffusion from the YBCO layer, during this step, we have set the etching current to its minimum (3 mA) [44, 58]. Moreover, to keep the etching homogeneous over all the sample through thermal conduction, 20 Torr of cooling He are applied under the platen. Temperature for the etching is kept fixed at circa room temperature with a water cooling system in function during etching.

Therefore the parameters that we have investigated are the angle of etching, α_{IBE} , and the time t_{IBE} .

With regards to the angle, we mostly considered for our fabrication two possibilities: 5° and 30° . This choice is mostly due to the fact that, while YBCO etches the fastest around 30° , due to the presence of 100 nm of carbon mask, it results in a much "softer", less energetic, way of creating the groove. In contrast, YBCO tends to etch slowly at 5° , but since the ions reach the surface almost perpendicularly, it results in an "aggressive" etching, for which a good percentage of material may never exit the nanogap and just end up being redeposited inside it.

This difference in the etching processes has allowed us to discover a second optimal area for electrical properties of GDBs for $\alpha_{IBE} = 30^\circ$, at much larger length: $l_{GDB} = 90 - 100nm$. In fact, by etching at a big angle, we can assume not only to be removing the redeposited material, which otherwise may recombine and contribute in lowering the superconducting properties of the weak link, but to have less unintentional damages caused by thermal effects. This would be further supported by the fact that, in average, 30° -etched GDBs appeared to show a much closer behavior to SS'S JJ, with a "rounder" shape of IVCs and smaller differential resistances with respect to 5° -etched GDBs.

With respect to the etching time t_{IBE} , instead, this parameter is inversely related to t_{GDB} . As it can be expected, the longer the etching, the thinner the superconducting material remaining inside the gap, until the gap turns resistive and finally an open circuit. To tune t_{IBE} is therefore fundamental in order to better select the electrical properties for GDB SQUIDS, in particular the I_c of the IVC. We found in this respect that we are able to "select" the required critical current by conducting additional steps of etching, even once the fabrication is terminated. This is a quite interesting development, since it allows for corrections on the I_c value *ex-situ*. In the next tables are shown the results of conducting two successive steps of ion milling, interspersed by IVC measurements at 77 K.

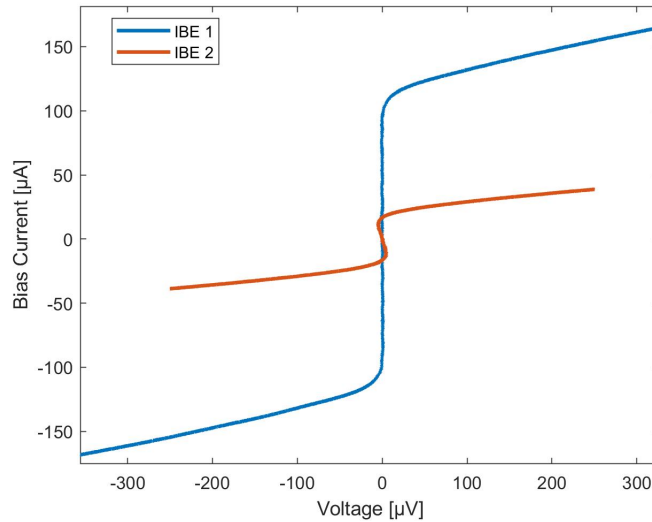
I_c [μm]	GDB1	GDB2	GDB3	GDB4
I_{c1}	173	101	597	501
I_{c2}	7.5	7.6	254	159

Table 3.3: Tables of IV results for 90/200, 100/200, 90/300 and 100/300 gaps after each two consecutive ion milling steps, of 1h 51 minutes and 10 minutes, respectively. Each value is found through averaging of 3 nominally identical devices critical currents)

I_c [μm]	GDB1	GDB2	GDB3	GDB4
I_{c1}	222	116	562	312
I_{c2}	110	35	440	197

Table 3.4: Tables of IV results for 90/200, 100/200, 90/300 and 100/300 gaps after each two consecutive ion milling steps, of 1h 12 min and 10 minutes, respectively. Each value is found through averaging of 3 nominally identical devices critical currents)

While this comparison does show that we can have a good degree of control over the critical current parameter by tuning t_{IBE} , it still needs to be mentioned that, the additional steps did not appear to affect the *shape* of the IVC curve.



(a)

Figure 3.6: Comparison of IVCs of a device prior and after an additional step of ion milling

This can be noticed in Fig. 3.6, where the same device is characterized between and after

two consecutive steps of ion milling and, while the I_c drops substantially, the IVC curve above it appears similar and not improved towards the typical RSJ shape, as we would expect with a device with improved electrical properties.

Therefore, we are not able to improve strongly the performances of the devices, connected instead more to their particular SNS or SS'S physics, by changing the etching time. Eventual additional steps of ion milling should then be seen as more of a fine tuning instrument on an already performant GDB SQUID, than an optimizing tool.

4 | Tuning of GDB electrical properties

As previously shown, nanowire-based SQUIDs, and in particular GDB-based ones, reach considerably good performances when the right parameters are chosen for the fabrication of weak links, making them suitable for several technological applications, such as magnetic field sensors. However, while these results are promising and associated to a much less complex fabrication process, at the moment GB-based SQUIDs are still characterised by the best performances. Indeed, the critical currents of nanowire-based devices are often too large and their values are subject to large fluctuations for nominally identical weak links [44].

Moreover, the performances of this type of device are further affected from an inevitable asymmetry of the critical currents of the two weak links, which cannot be corrected during fabrication, and that can frequently lead to a reduction of voltage modulation depth ΔV or even to their complete suppression and, therefore, to an increase of the overall flux noise.

For this reason, we went beyond fabrication optimization and searched for new ways of tuning the weak links electrical properties, to further improve the nanowire-based SQUIDs performances. Oxygen electromigration [EM] of weak links is one of them and the one that was most successful during this work.

4.1. Electromigration: tuning of Oxygen doping

Tuning the hole doping of YBCO through electromigration (EM) of oxygen was first studied for thin films and GB junctions, and it has seen recent advancements also for YBCO nanowires [59–61]. The promising results of this technique opened up the possibility to locally modify *ex-situ* the electrical properties of YBCO nanowire based SQUIDs, similarly to what was already done with LTS-based SQUIDs.

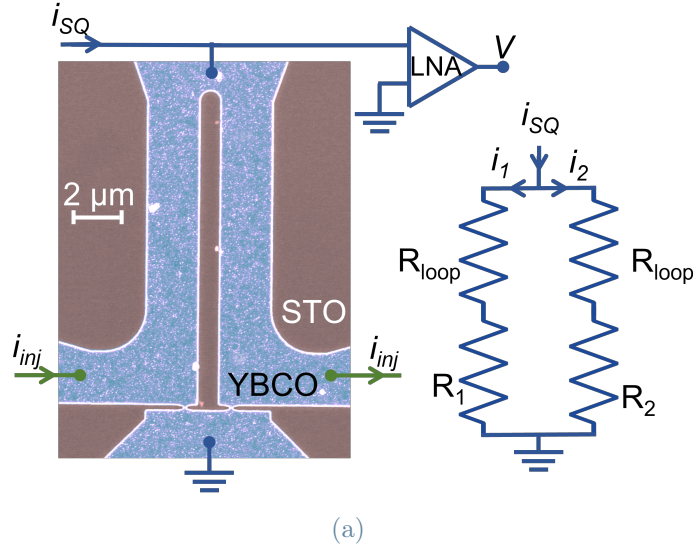


Figure 4.1: EM typical setup. On the left, a SEM picture of a SQUID connected to the system for EM. On the right, the related simplified circuit scheme

In Fig. 4.1 is shown a SEM image of a nanowire-based SQUID, with a simplified scheme of the electromigration experiment setup. The top and the bottom electrodes are connected to a signal generator, which normally provides the SQUID with a bias current i_{SQ} , and to a low noise amplifier, which measures the voltage drop V over the SQUID. In the context of an EM tuning experiment, that current will be substituted with the EM current. The SQUID loop is connected to a second source as well, which is used for current injection i_{inj} to modulate the phase difference between the two weak links $\Delta\varphi$.

On the right, an equivalent circuit of the SQUID in its normal state, i.e. above critical temperature, is shown as well. In that, it needs to be made the distinction between the macroscopic size (μm) arms of the SQUID loop, which can be assumed to have the same resistance and equal to R_{loop} , and the resistance of the two nanowires, R_1 and R_2 . Since the weak links are built approaching the limits of fabrication, their resistances could be different and introduce as a consequence an asymmetric component in the distribution of current. Indeed, while in the normal state, if $R_1 = R_2$ then $i_1 = i_2 = i_{SQ}/2$, while if $R_1 > R_2$, then $i_1 < i_2$ and viceversa. This effect is relevant in the context of DC-EM, which was done at room temperature and whose purpose was to effectively reduce such an asymmetry. On the other hand, AC-EM is usually conducted at liquid nitrogen temperature, therefore should not suffer from this problem.

Moreover, EM (whether at room or at liquid nitrogen temperature) was found to be strongly dependant on the value of local current density, so that where constrictions and

related current crowding effects are present, the effects of EM will be much increased, as will be made clear by the results presented in the following sections.

More in detail on the two kind of EM:

DC-Electromigration: it was first tried to tune the doping of the oxygen of the YBCO nanostructures through the application of a dc current density in the range 7-15 MAcm⁻² [62]. The result could be a reduction of the doping, as well as a replenish of it, increasing therefore the screening parameter of the nanostructures. However, in this case this processes were found to happen in a rather inhomogeneous way along the weak link and to give, as a consequence, not fully satisfying results. For this reason, this technique for the electromigration was only experimented first on bare nanowires, as shown later in the chapter.

AC-Electromigration: On the other hand, a very effective tuning of doping for operations at 77 K can be done through AC-type electromigration. AC-EM can be achieved by applying an ambipolar square wavefunction at 1kHz, with an amplitude above 17 MAcm⁻² [62]. The effects of it on the nanowire's critical current can be divided into two main regimes, depending on the current amplitude that is applied across the weak link:

An "healing" regime [lower values of the current, circa 0.25-0.30 mA], where the critical current I_c can be slowly increased with respect to its original value, up to a 10 percent. In this regime we hypothesize that oxygen is moved from the electrodes to the constriction, where it appears to compensate for the possible oxygen losses that may have happened during fabrication. We believe that in this regime it is possible to "heal" eventual defects that may have been generated along the weak link and, as such, to compensate for possible asymmetries that may have developed during fabrication.

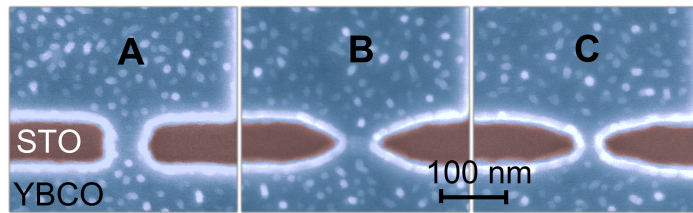
A "degradation" regime [higher values of the current, above 0.45 mA], where the critical current of the weak link can be strongly reduced (down to even a few μ A) and the shape of the IV characteristics can be modified to resemble more the RSJ model. Moreover, while I_c decreases, the differential resistance increases, thus possibly increasing the performances of the specific device. However, is worth noticing that there is not fixed minimum voltage to access this regime: such value depends indeed strongly on the type of constriction we are applying it to. Not only that, but the behavior of the I_c in this regime varies much between same-type devices, depending on their initial conditions, and even more between different kinds of nanowire-like weak links. While in this regime, it is believed that the electrical pulses deplete the constriction of oxygen, increasing as a consequence the difference in superconducting behavior between the weak link and the electrodes and hopefully improving the performances of the device. Underneath the "healing" regime no

permanent changes happen to the electrical properties of the weak links, while above the "degradation" regime the weak link becomes resistive or may even explode (due to thermal runaway), suppressing completely the voltage modulations, usually in an irreparable way.

In the following section, the effects we found of EM on the voltage modulations of YBCO nanowire-based SQUIDs will be presented. First of all, the results on bare nanowire weak links, which have been used as a guide for further experiments, and lastly, what we were able to achieve for the GDB weak links.

4.2. Electromigration tuning of nanowire-based SQUID devices

For a first exploratory EM experimentation on nanowire-based weak links, we fabricated SQUIDs based on three different geometrical profiles, to best take advantage of the strong correlation between EM and current crowding around constrictions in the material.



(a)

Figure 4.2: SEM images, colour corrected, of nanowire profiles on which electromigration was tested. SQA is a classical nanowire, SQB a more "constricted" version of it, also called "point contact". SQC a point contact with corners removed from profile.

In figure 4.2 are compared the SEM images of the three types of weak link: type A refers to rectangular shaped nanowires with a 2:1 aspect ratio, while type B and C are designed constrictions with the aim of concentrating the EM effects in the narrowest possible region. As a plus, they have a reduction of the overall parasitic kinetic inductance as well [63].

To study the EM effects on the performance of the devices, we monitored the voltage modulation depth ΔV while repeating the same EM steps on all the devices and characterizing them at 77 K before and after each step.

During this particular work, the SQUIDs critical current and modulation depth are measured directly after fabrication, then a DC-EM step is conducted at room temperature; afterwards, the devices undergo two steps of AC-EM at LN_2 temperature. For the step

	<i>Before</i>	<i>EM</i>	<i>DC</i>		<i>AC₁</i>		<i>AC₂</i>	
	I_c	ΔV	I_c	ΔV	I_c	ΔV	I_c	ΔV
<i>SQA</i>	580	-	550	0.2	190	1	110	1.7
<i>SQB</i>	700	-	700	0.7	610	1.5	330	1.8
<i>SQC</i>	500	0.7	510	0.7	150	5	100	4.7

Table 4.1: Electromigration results for DC and AC steps on nanowire weak links with different constriction profiles, SQA, SQB and SQC.

of DC, aimed to replenish the nanowires with oxygen, the current bias is applied to the SQUID and then manually increased. The successive steps of AC-EM (referred to as AC1 and AC2), aimed instead at reducing the critical current, are performed by applying a square wavefunction centered around zero, with frequency of 1 kHz. This value is chosen in order to exclude motion of the oxygen atoms due to the AC current, In fact, the period of the current results to be much smaller than the relaxation time constant for diffusion of oxygen in the working conditions, ($\tau \simeq 400s$), therefore motion of oxygen in the wire is fully due by thermomigration. Here, a large temperature gradient between electrodes dominates over the oxygen migration in between [64]. The AC bias current will be applied in the form of pulses, of 100 ms duration each.

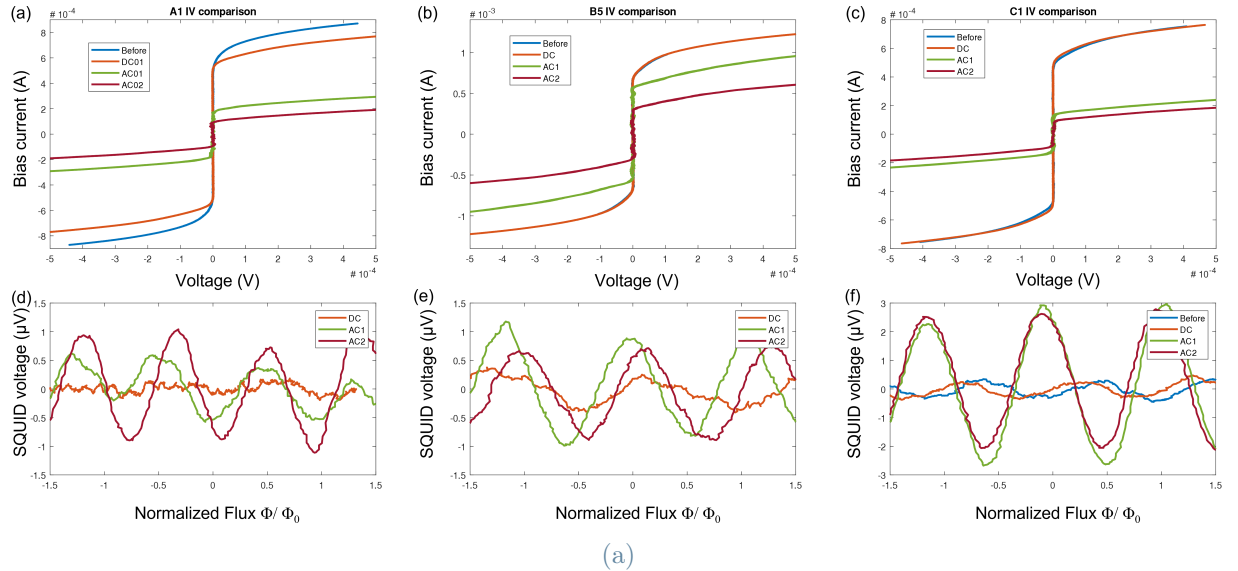


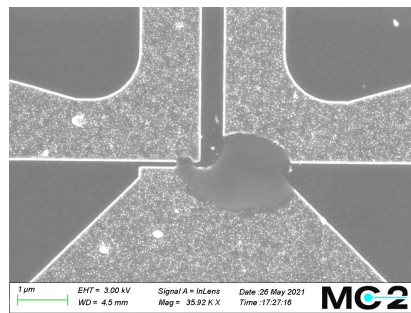
Figure 4.3: EM of nanowire-based SQUIDs with respect to the evolution of their electrical properties. IVC and δR of SQA, SQB and SQC are shown.

In the table 4.1 the results in terms of IVC are presented for each step, and related curve is found in Fig. 4.3. In both cases the results corresponding to the voltage modulations versus normalized applied magnetic flux are presented as well (δV). The absent voltage

modulations correspond to measurements where their amplitude was below the noise limit of our experimental setup.

From the results of the first step, of DC-Em, we notice an increase of δV for SQA and SQB types, since their modulations rise above the noise level. This could be maybe attributed to an improved critical current symmetry of the weak links, due to the "healing" of oxygen that is conducted inside the groove. For SQC, where there was no detectable improvement, we may assume that the critical current values of the weak links were already comparable before the EM step.

On the other hand, drastic changes came as a result of each AC-EM step. The main effects we encountered were a reduction of the critical current, associated however with a differential resistance increase. This implied strong increases in the voltage modulations, up to a factor 8 for SQA and a factor 7 for SQC. The voltage modulations of SQB were the ones to improve the less, only by a factor 2, and it is mostly due to the limited decrease that could be induced in the critical current, while avoiding breaking superconductivity. Indeed, for the second type of weak links, I_c could only be reduced by a factor $\simeq 2$ before degradation of weak links would start rapidly accelerating and eventually lead to the loss of all its superconductive properties. The fast degradation of SQB with AC-EM is related to the fact that, due to strong central constriction, the current density will be higher there, especially on the inner corners, where current crowding is enhanced. This results in a critically high electric field that limits the control over the AC-EM process for this weak link type. If we push the process any further, the electromigration of the weak link would result in a thermal runaway and irreversible damage. In some cases, that may lead even to its "explosion" (Fig. 4.5).



(a)

Figure 4.4: SEM image of a nanowire-based SQUID after an electromigration step. The picture shows one of the possible destructive consequence of AC-electromigration on nanostructures.

While SQC have a similar constriction profile, the design is done to avoid current crowding on the inner corners, therefore the different results.

The main effect that was found for AC-EM was to reduce the nanowire doping, by thermomigration of oxygen, which influences the critical temperature T_c , the London penetration depth and coherence length of the weak link. Most relevant is however the T_c reduction, since, as explained previously, YBCO properties change drastically at temperatures close to T_c . We can then correlate directly T_c value to the level of doping inside the weak links, assuming the other superconducting properties to change much less in comparison, and find as a consequence the correlation between T_c and ΔV modulations:

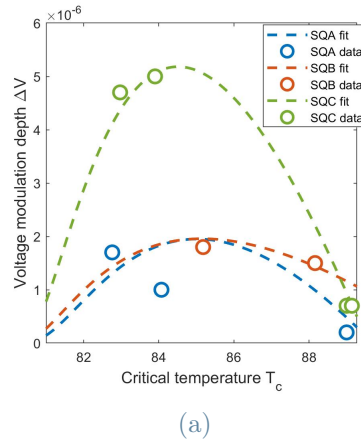


Figure 4.5: Correlation of measured voltage modulation depth of SQA, SQB and SQC, and the critical temperature of superconductor in the weak link. An optimal point was found to increase voltage performances.

For all of three SQUIDS we found that ΔV first increases with decreasing critical temperature of weak links, due to the screening parameter reduction and increase of differential resistance. However, for $T_c = 85K$ the voltage modulations start decreasing again, even though β_L continues to decrease. That is a consequence of T_c reaching the bath temperature of LN_2 , when then the weak link I_c goes to zero (as seen in ch.3) and therefore ΔV as well.

As a conclusion, we noticed from this experiment of optimization through EM tuning, that we are able to improve the performances of SQUID devices and that the best results are obtained for the nanowires with gradual reduction of the central part. Therefore, we derive that for the weak links with a constriction-type of profile we can expect for the technique to give the best results.

Due to the profile similarities then, we expect for GDBs to have ΔV increments as well

	<i>Before</i>	<i>EM</i>	<i>AC</i> ₁		<i>AC</i> ₂		<i>AC</i> ₃		<i>AC</i> ₄	
	I_c	ΔV	I_c	ΔV	I_c	ΔV	I_c	ΔV	I_c	ΔV
<i>SQ1</i>	720	-	600	2	500	2.3	293	1.5	444	2.3
<i>SQ2</i>	358	2	358	9.1					358	8.7
<i>SQ3</i>	232	4	190	15	140	23	110	18	208	10
<i>SQ4</i>	59	5	59	8	59	13			59	5
<i>SQ5</i>	218	10	140	17.5	160	18	160	16	200	11

Table 4.2: Table of results for AC-electromigration on GDB-based SQUIDs. *SQ1*, *SQ3* and *SQ5* refer to AC with aim of reducing I_c . On *SQ2* and *SQ4* instead, I_c was kept fixed and shape of IVC refined. Last column is reserved for electrical characterization after one thermal cycling.

and, therefore, to be able to optimize ex-situ GDB-based SQUIDs thanks to the electromigration technique.

4.2.1. Electromigration tuning of GDB-based SQUID devices

After the encouraging results of nanowire weak links with EM, we repeated the experiment with GDBs. However, we chose to not have a DC-EM step, due to the fact that most of the improvement appeared to come from the AC-EM steps, implying that the asymmetry between weak links may not be too much of a determining factor with respect to I_c and δR in the end result for performances.

The parameters for AC-EM are maintained the same as the previous section, as well as the characterization process. In this case, however, three steps of AC-EM were conducted, each followed and preceded by IVC and δR measurements. The first three consecutively done at 77 K, the last after a thermal cycle, where the device is brought up to room temperature and cooled again to LN_2 bath temperature. The latter step was performed in order to evaluate the stability of the results obtained with the precedent steps. Lastly, a noise measurement was conducted on the best performing device in a magnetically isolated chamber.

In the table 4.2 are reported some of the results, written with respect to the gaps geometrical dimensions.

The gaps chosen were all in the range $l_{GDB} = 30 - 50nm$ and $w_{GDB} = 200 - 300nm$, optimal area found for geometrical dimensions of GDB-based SQUIDs.

Two types of investigations with AC-DC were conducted on this devices: "reshaping" of IVC and lowering of critical current in the degradation regime.

Reshaping EM focus was on the behavior of IVC for bias just above I_c . While reshaping, we were not interested in changing the critical current value and kept therefore the current density of pulses around the value for which the degradation regime started. This adds however another level of complexity to the experiment, since it is not possible to find a common value for the minimum current density that starts the degradation of the weak links. Indeed, it was found to strongly depend on the specific GDB dimensions and condition of the YBCO film in the groove, where the constriction is at its maximum and, therefore, the crowding effect caused by EM current. The results for this investigation were substantial: while the I_c was not changed by definition of the process, δR seemed to be strongly affected by the shape of the IVC curve, and therefore ended up adding a positive contribution to the depth of the voltage modulations of the device. SQ2 and SQ4 are example of the results for this technique, by showing at maximum an improvement in ΔV of almost 4 times the original one. In Fig. 4.6, IVC and δR changes induced by the first step of AC-EM are plotted for the SQ2 device. With a very minimal modification in the curve shape above I_c , we gained more than triple the initial value of ΔV .

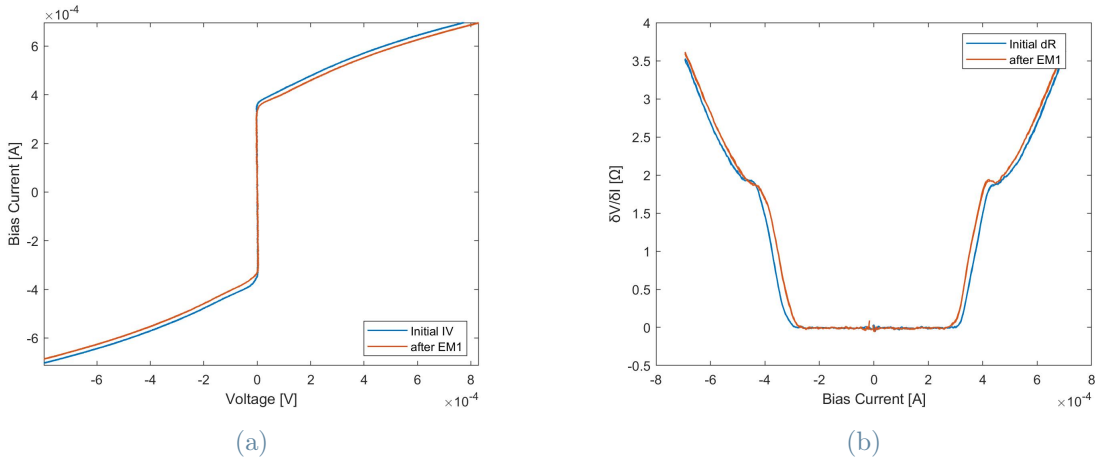


Figure 4.6: IVC and δR results of "reshaping" AC-EM on SQ2. While the changes in these graphs are almost noticeable, ΔV increase was substantial and mostly maintained after thermal cycling

AC-EM in the degradation regime is instead more similarly done with respect to the AC-EM conducted on nanowires. However, as happened for SQB, GDB run the risk of thermal runaway due to the constriction profile with inner corners where current crowding can happen and destroy superconductivity. This time, we were able to counteract this effect by waiting a "stabilization" time at a fixed current intensity, before proceeding to increase the amplitude of the pulses. Supposedly, by waiting at fixed EM current for an

amount of time long enough, we allow for the effects of the previous, lower energy pulses of electromigration to settle, and therefore we are able to see the IVC and δR response before taking further action. Besides these corrections, we may assume that the results of EM for ΔV follow the same physics as the one of SQB of the previous electromigration tuning. SQ1, SQ3 and SQ5 in table have been electromigrated following this second procedure, where SQ3 was found to be the most performing device, with an increase of almost 6 times the initial ΔV for a reduction of the I_c of not even half the original values. The IVC and ΔV have been plotted hereby for completeness:

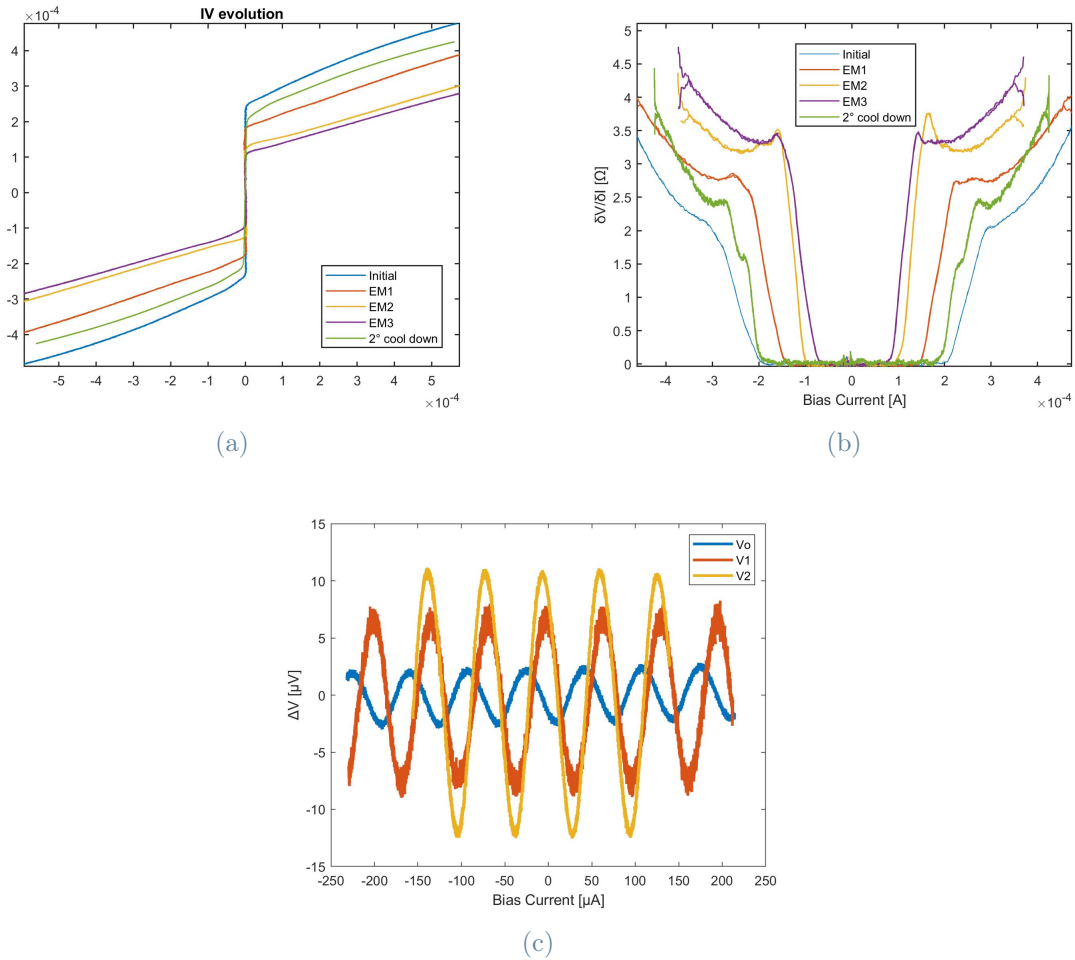


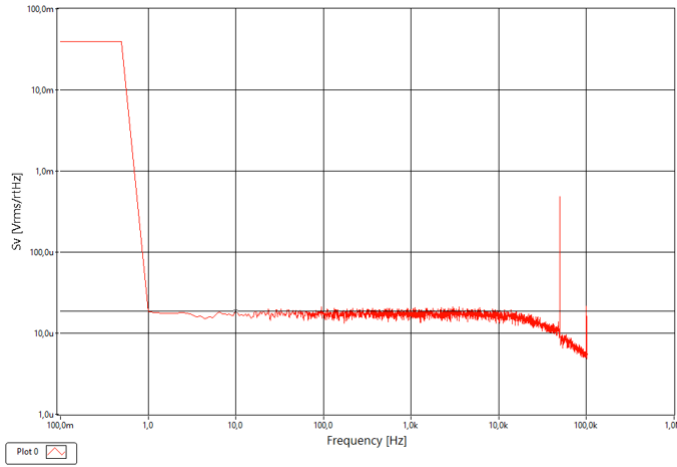
Figure 4.7: Best results obtained for electromigration tuning on a GDB SQUID, SQ3. (a) and (b) are the IVC and differential resistance, respectively. (c) plots the evolution of the voltage modulations with respect to the EM steps 1 and 2.

After the second step of AC-EM, however, we found that ΔV does not increase any further for decreasing I_c , but starts instead losing amplitude. We conclude from this that there is a maximum for ΔV , as was found for nanowires. Once passed that, the superconductive

temperature T_c in the groove may start approaching the bath temperature, and therefore the GDB may start losing its superconductive properties.

Once completed the third step of AC, we effectuated a thermal cycle. The purpose was, as mentioned above, to understand if the improvements added with EM tuning of the gaps were able to withstand the change in temperature. Indeed, we assume that at room temperature the oxygen motion may be thermally re-activated, but in the opposite direction: the gradient in doping levels generated by the EM action between the nanogap and the electrodes, may be in fact sufficient to stimulate a "re-population" of oxygen atoms in the groove. And while this effect was found, therefore causing in most SQUIDs a loss of Δv , along with an increase in I_c , it was only partial. In particular, for the SQUIDs in which EM steps had been conducted with the "stabilization" waiting time, most of the improvement in ΔV was found to be conserved through the thermal cycle (example in table, SQ1).

Lastly, a flux noise measurement on the most optimally tuned GDB SQUID was done, in order to evaluate the effect of AC-EM on the devices.



(a)

Figure 4.8: Noise measurement on the most performing electromigrated GDB, SQ3. Even after 3 steps of electromigration and a thermal cycling, no deviation of noise value from optimized samples was found.

The process of AC-EM was in fact expected to introduce significant disorder in the weak links, which would give additional noise sources. For investigation of the magnetic flux noise of the SQUID, we brought it in a magnetic shielded room and used a commercial Magnicon SEL-1 dc-SQUID electronics, operated in flux-locked loop and bias reversal mode (40 kHz), the latter to reduce the 1/f contribution. The result, measured at 77

K and shown in Fig.4.8 is the following: no sensible increase in the flux noise could be detected, considering that, at $7 \mu\Phi_0/\sqrt{Hz}$ for the white magnetic flux noise above the $1/f$ knee, given the amplifier input voltage noise of $0.4 nV/\sqrt{Hz}$ and a transfer function of $\pi\Delta V \simeq 30\mu V/\Phi_0$, it appeared to mainly come from the system electronics. That is perfectly in line with optimized GDB SQUIDs fabricated before [26].

5 | Conclusions and future developments

During this thesis work, we have fabricated and characterized a few hundreds of GDB-based, YBCO SQUIDS. And while the fabrication mostly followed an already traced and verified path, we were able to experiment with a few key parameters of it, such as the carbon mask height or the etching conditions, and modify them with respect to transport considerations we derived from IVCs and differential resistances of the devices. In this way, we were able to understand how certain aspects of fabrication directly effect the resulting properties of GDB SQUIDS, and it led us to find, for an etching angle of 30° , a second optimal area for GDB geometrical dimensions at $l=90-100$ nm and $w=200-300$ nm, which presented quite similar electrical properties with respect to GDB fabricated by etching at 5° , with $l=40-50$ nm and $w=200-300$ nm.

However, the improvements obtained from this *in-situ* optimization, while they were there, were often minimal and not at all sufficient to close the gap in sensitivity between GDB and the state-of-art JJ for SQUID applications, the Grain Boundary. $I_c R_N$ resulted in line with what it was already obtained in past works and, therefore, still less performing than GB-based SQUIDS. The insufficiency of these results is most noticeable in the context of sensing application, such as SQUID magnetometers. In fact, we found that, while we obtain more reliable results with magnetometers by using SQUIDS with 90-100 nm grooves, they do not present sufficiently enhanced voltage modulations to perform above the level of noise of our instrumentation, with very few exceptions.

In this regard, we believe most of the issue steams from our inability during fabrication to control the damage done in the groove. A possible *in-situ* solution to this, would be to add a step of Focused Ion Beam (FIB) towards the end of the process. Indeed, given the very small width that can be achieved for the beam (0.5 nm) and, therefore, the possibly very small irradiation area of the weak link, this technique has the potential of adding to the process a great level of precision that could be exactly what it is currently missing from it. In fact, it could be inserted after a complete fabrication of GDBs with grooves

etched at 30° , where, as a last step, a FIB irradiation is done in the position of the groove to introduce *intentional, controlled damage*.

Different are the conclusions for the results of *ex-situ* tuning, thanks to the electromigration (EM) technique. This technique, and in particular AC-EM, even if it is still at its early stages of application on SQUIDs, appears to be giving very promising results and to be, hopefully, key to future substantial development. In fact, it performed well with nanowire-like weak links, by giving ΔV increases up to 8 times the original value, although it did so on poorly performing devices (ΔV under noise level or up to $2\text{-}3\ \mu\text{V}$) and often at the price of irreversible damage. On the other hand, when the technique was applied again on GDB SQUIDs, the results were even more encouraging. Not only we were able to find improvements of ΔV up to 6 times the original value, but they were obtained without needing to induce strong decreases in critical current, which can often be associated to inevitable damage done to the weak links. Moreover, it was able to greatly improve performances of already well modulating devices.

This finding has the opportunity to substantially better the achievements that have been reached with GDBs and their technological applications, to the point of possibly rendering them truly effective even in the sensing field. Nevertheless, one of the objectives of next future research with EM, will need to be to create a standard protocol for the process, with focus on the reproducibility of it and the results obtainable, with particular attention as well on finding a solution in order to maintain the achieved performances after thermal cyclings. Currently, in fact, while not all the progress is lost when the device is brought to room temperature, a part of it is, and that makes challenging to have a reliable electrical characterization for electromigrated samples. Therefore, in order to fully benefit from such a technique, a better understanding of the process is necessary and possible ways to avoid the redistribution of oxygen need to be found.

In conclusion, much has been done to reach the point of optimization at which GDB-based SQUIDs are now, but much more could still be improved. *In-situ* techniques such as FIB and *ex-situ* ones as EM have the potential to strongly affect the performances of these nanostructures and, as a consequence, to make them truly competitive in technological applications with the state-of-art and, maybe, to even reach beyond them. Such an achievement could be pivotal in progressing some SQUID-based research areas, mostly the ones in which, having an increased range of temperatures and magnetic fields, could truly make the difference.

Bibliography

- [1] O. H. KAMERLINGH, “The resistance of pure mercury at helium temperatures,” *Commun. Phys. Lab. Univ. Leiden, b*, vol. 120, 1911.
- [2] W. Meissner and R. Ochsenfeld, “Ein neuer effekt bei eintritt der supraleitfähigkeit,” *Naturwissenschaften*, vol. 21, no. 44, pp. 787–788, 1933.
- [3] F. London and H. London, “The electromagnetic equations of the supraconductor,” *Proc. R. Soc. Lond. A Math. Phys. Sci.*, vol. 149, no. 866, pp. 71–88, 1935.
- [4] V. L. Ginzburg and L. Landau, “On the theory of superconductivity (1950),” *Supercond. Superfluidity*, pp. 113–137, 1965.
- [5] J. Bardeen, L. N. Cooper, and J. R. Schrieffer, “Theory of superconductivity,” *Phys. Rev.*, vol. 108, no. 5, p. 1175, 1957.
- [6] J. G. Bednorz and K. A. Müller, “Possible high T_c superconductivity in the $Ba - La - Cu - O$ system,” *Zeitschrift für Physik B Condensed Matter*, vol. 64, no. 2, pp. 189–193, 1986.
- [7] A. A. Abrikosov, “The magnetic properties of superconducting alloys,” *Journal of Physics and Chemistry of Solids*, vol. 2, no. 3, pp. 199–208, 1957.
- [8] R. Arpaia, *YBa₂Cu₃O_{7- δ} nanowires to study nanoscale ordering in High - T_c Superconductors*. PhD thesis, Chalmers Tekniska Hogskola, Gothenburg, Sweden, 2016.
- [9] J. Jorgensen, B. Veal, A. P. Paulikas, L. Nowicki, G. Crabtree, H. Claus, and W. Kwok, “Structural properties of oxygen-deficient $YBa_2Cu_3O_{7-\delta}$,” *Phys. Rev. B*, vol. 41, no. 4, p. 1863, 1990.
- [10] W. E. Pickett, “Electronic structure of the high-temperature oxide superconductors,” *Rev. Mod. Phys.*, vol. 61, no. 2, p. 433, 1989.
- [11] Y. Tokura and T. Arima, “New classification method for layered copper oxide compounds and its application to design of new high T_c superconductors,” *Jpn. J. Appl. Phys.*, vol. 29, no. 11R, p. 2388, 1990.

- [12] H. Smilde, A. A. Golubov, G. Rijnders, J. Dekkers, S. Harkema, D. Blank, H. Rogalla, H. Hilgenkamp, *et al.*, “Admixtures to d-wave gap symmetry in untwinned $YBa_2Cu_3O_7$ superconducting films measured by angle-resolved electron tunneling,” *Phys. rev. lett.*, vol. 95, no. 25, p. 257001, 2005.
- [13] E. Wahlberg, *Reshaping the phase diagram of $YBa_2Cu_3O_{7-\delta}$ through strain in ultrathin films and nanowires*. PhD thesis, Chalmers Tekniska Hogskola, Gothenburg, Sweden, 2021.
- [14] R. Liang, D. Bonn, and W. Hardy, “Evaluation of CuO_2 plane hole doping in $YBa_2Cu_3O_{6+x}$ single crystals,” *Phys. Rev. B*, vol. 73, no. 18, p. 180505, 2006.
- [15] J. Orenstein, J. Schrieffer, and J. Brooks, “Handbook of high-temperature superconductivity,” 2007.
- [16] J. Chang, E. Blackburn, A. Holmes, N. B. Christensen, J. Larsen, J. Mesot, R. Liang, D. Bonn, W. Hardy, A. Watenphul, *et al.*, “Direct observation of competition between superconductivity and charge density wave order in $YBa_2Cu_3O_{6.67}$,” *Nat. Phys.*, vol. 8, no. 12, pp. 871–876, 2012.
- [17] B. Keimer, S. A. Kivelson, M. R. Norman, S. Uchida, and J. Zaanen, “From quantum matter to high-temperature superconductivity in copper oxides,” *Nature*, vol. 518, no. 7538, pp. 179–186, 2015.
- [18] A. Abrikosov, Alekseï, *Fundamentals of the Theory of Metals*. Courier Dover Publications, 2017.
- [19] Y. Sato, S. Kasahara, H. Murayama, Y. Kasahara, E.-G. Moon, T. Nishizaki, T. Loew, J. Porras, B. Keimer, T. Shibauchi, *et al.*, “Thermodynamic evidence for a nematic phase transition at the onset of the pseudogap in $YBa_2Cu_3O_y$,” *Nat. Phys.*, vol. 13, no. 11, pp. 1074–1078, 2017.
- [20] G. Ghiringhelli, M. Le Tacon, M. Minola, S. Blanco-Canosa, C. Mazzoli, N. Brookes, G. De Luca, A. Frano, D. Hawthorn, F. He, *et al.*, “Long-range incommensurate charge fluctuations in $(Y, Nd)Ba_2Cu_3O_{6+x}$,” *Science*, vol. 337, no. 6096, pp. 821–825, 2012.
- [21] R. Arpaia, S. Caprara, R. Fumagalli, G. De Vecchi, Y. Peng, E. Andersson, D. Betto, G. De Luca, N. Brookes, F. Lombardi, *et al.*, “Dynamical charge density fluctuations pervading the phase diagram of a Cu -based high- T_c superconductor,” *Science*, vol. 365, no. 6456, pp. 906–910, 2019.

- [22] R. Arpaia and G. Ghiringhelli, “Charge order at high temperature in cuprate superconductors,” *J. Phys. Soc. Jpn.*, vol. 90, no. 11, p. 111005, 2021.
- [23] V. Hinkov, D. Haug, B. Fauqué, P. Bourges, Y. Sidis, A. Ivanov, C. Bernhard, C. Lin, and B. Keimer, “Electronic liquid crystal state in the high-temperature superconductor $YBa_2Cu_3O_{6.45}$,” *Science*, vol. 319, no. 5863, pp. 597–600, 2008.
- [24] D. Haug, V. Hinkov, Y. Sidis, P. Bourges, N. B. Christensen, A. Ivanov, T. Keller, C. Lin, and B. Keimer, “Neutron scattering study of the magnetic phase diagram of underdoped $YBa_2Cu_3O_{6+x}$,” *New J. Phys.*, vol. 12, no. 10, p. 105006, 2010.
- [25] B. D. Josephson, “Possible new effects in superconductive tunnelling,” *Phys. Lett.*, vol. 1, no. 7, pp. 251–253, 1962.
- [26] E. Tralbaldo, *Noise and electrical properties of YBCO nanostructures*. PhD thesis, Chalmers Tekniska Hogskola, Gothenburg, Sweden, 3 2020.
- [27] J. Clarke and A. I. Braginski, “The squid handbook. vol.2. applications of squids and squid systems,” 2006.
- [28] W.-T. Tsang and T. Van Duzer, “Dc analysis of parallel arrays of two and three josephson junctions,” *J. Appl. Phys.*, vol. 46, no. 10, pp. 4573–4580, 1975.
- [29] K. Hasselbach, D. Mailly, and J. Kirtley, “Micro-superconducting quantum interference device characteristics,” *J. Appl. Phys.*, vol. 91, no. 7, pp. 4432–4437, 2002.
- [30] M. Faucher, T. Fournier, B. Pannetier, C. Thirion, W. Wernsdorfer, J. Villegier, and V. Bouchiat, “Niobium and niobium nitride squids based on anodized nanobridges made with an atomic force microscope,” *Physica C: Superconductivity*, vol. 368, no. 1–4, pp. 211–217, 2002.
- [31] R. H. Koch, J. Clarke, W. Goubau, J. M. Martinis, C. Pegrum, and D. J. Van Harlingen, “Flicker ($1/f$) noise in tunnel junction dc squids,” *J. Low Temp. Phys.*, vol. 51, no. 1, pp. 207–224, 1983.
- [32] V. Foglietti, W. Gallagher, M. Ketchen, A. Kleinsasser, R. Koch, S. Raider, and R. Sandstrom, “Low-frequency noise in low $1/f$ noise dc squid’s,” *Appl. Phys. Lett.*, vol. 49, no. 20, pp. 1393–1395, 1986.
- [33] J. Malmivuo, J. Lekkala, P. Kontro, L. Suomaa, and H. Vihinen, “Improvement of the properties of an eddy current magnetic shield with active compensation,” *Journal of Physics E: Scientific Instruments*, vol. 20, no. 2, p. 151, 1987.

- [34] C. D. Tesche and J. Clarke, “Dc squid: Noise and optimization,” *J. Low Temp. Phys.*, vol. 29, no. 3, pp. 301–331, 1977.
- [35] H. Hilgenkamp and J. Mannhart, “Grain boundaries in high- T_c superconductors,” *Rev. Mod. Phys.*, vol. 74, no. 2, p. 485, 2002.
- [36] D. Dimos, P. Chaudhari, J. Mannhart, and F. LeGoues, “Orientation dependence of grain-boundary critical currents in $YBa_2Cu_3O_{7-\delta}$ bicrystals,” *Phys. Rev. Lett.*, vol. 61, no. 2, p. 219, 1988.
- [37] K. Daly, W. Dozier, J. Burch, S. Coons, R. Hu, C. Platt, and R. Simon, “Substrate step-edge $YBa_2Cu_3O_7$ rf squids,” *Appl. Phys. Lett.*, vol. 58, no. 5, pp. 543–545, 1991.
- [38] K. Char, M. Colclough, S. Garrison, N. Newman, and G. Zaharchuk, “Bi-epitaxial grain boundary junctions in $YBa_2Cu_3O_7$,” *Appl. Phys. Lett.*, vol. 59, no. 6, pp. 733–735, 1991.
- [39] M. Faley, J. Dammers, Y. Maslennikov, J. Schneiderman, D. Winkler, V. Koshelets, N. Shah, and R. Dunin-Borkowski, “High- T_c squid biomagnetometers,” *Supercond. Sci. Technol.*, vol. 30, no. 8, p. 083001, 2017.
- [40] U. Poppe, Y. Divin, M. Faley, J. Wu, C. Jia, P. Shadrin, and K. Urban, “Properties of $YBa_2Cu_3O_7$ thin films deposited on substrates and bicrystals with vicinal offcut and realization of high $I_c R_n$ junctions,” *IEEE Trans. Appl. Supercond.*, vol. 11, no. 1, pp. 3768–3771, 2001.
- [41] G. Clark, A. Marwick, R. Koch, and R. Laibowitz, “Effects of radiation damage in ion-implanted thin films of metal-oxide superconductors,” *Appl. Phys. Lett.*, vol. 51, no. 2, pp. 139–141, 1987.
- [42] B. Müller, M. Karrer, F. Limberger, M. Becker, B. Schröppel, C. Burkhardt, R. Kleiner, E. Goldobin, and D. Koelle, “Josephson junctions and squids created by focused helium-ion-beam irradiation of $YBa_2Cu_3O_7$,” *Phys. Rev. Appl.*, vol. 11, no. 4, p. 044082, 2019.
- [43] P. Anderson and A. Dayem, “Radio-frequency effects in superconducting thin film bridges,” *Phys. Rev. Lett.*, vol. 13, no. 6, p. 195, 1964.
- [44] S. Nawaz, R. Arpaia, T. Bauch, and F. Lombardi, “Approaching the theoretical depairing current in $YBa_2Cu_3O_{7-\delta}$ nanowires,” *Physica C*, vol. 495, pp. 33–38, 2013.
- [45] R. Arpaia, M. Arzeo, S. Nawaz, S. Charpentier, F. Lombardi, and T. Bauch, “Ultra

- low noise $YBa_2Cu_3O_{7-\delta}$ nano superconducting quantum interference devices implementing nanowires,” *Appl. Phys. Lett.*, vol. 104, no. 7, p. 072603, 2014.
- [46] R. Arpaia, M. Arzeo, R. Baghdadi, E. Trabaldo, F. Lombardi, and T. Bauch, “Improved noise performance of ultrathin ybco dayem bridge nanosquids,” *Supercond. Sci. Technol.*, vol. 30, no. 1, p. 014008, 2016.
- [47] E. Trabaldo, R. Arpaia, M. Arzeo, E. Andersson, D. Golubev, F. Lombardi, and T. Bauch, “Transport and noise properties of ybco nanowire based nanosquids,” *Supercond. Sci. Technol.*, vol. 32, no. 7, p. 073001, 2019.
- [48] K. Likharev, “Superconducting weak links,” *Rev. Mod. Phys.*, vol. 51, no. 1, p. 101, 1979.
- [49] M. Tinkham, *Introduction to superconductivity*. Courier Corporation, 2004.
- [50] R. Arpaia, D. Golubev, R. Baghdadi, R. Ciancio, G. Dražić, P. Orgiani, D. Montemurro, T. Bauch, and F. Lombardi, “Transport properties of ultrathin $YBa_2Cu_3O_{7-\delta}$ nanowires: A route to single-photon detection,” *Phys. Rev. B*, vol. 96, no. 6, p. 064525, 2017.
- [51] G. Alvarez, K. Taylor, and G. Russell, “Josephson behaviour of variable thickness bridges in textured $YBa_2Cu_3O_{7-\delta}$,” *Physica C*, vol. 165, no. 3-4, pp. 258–264, 1990.
- [52] E. Trabaldo, C. Pfeiffer, E. Andersson, R. Arpaia, A. Kalaboukhov, D. Winkler, F. Lombardi, and T. Bauch, “Grooved dayem nanobridges as building blocks of high-performance $YBa_2Cu_3O_{7-\delta}$ squid magnetometers,” *Nano Lett.*, vol. 19, no. 3, pp. 1902–1907, 2019.
- [53] D. Koelle, R. Kleiner, F. Ludwig, E. Dantsker, and J. Clarke, “High-transition-temperature superconducting quantum interference devices,” *Rev. Mod. Phys.*, vol. 71, 1999.
- [54] D. Cohen, E. A. Edelsack, and J. E. Zimmermann, “Magnetocardiogram taken inside a shielded room with a superconducting point-contact magnetometer,” *Appl. Phys. Lett.* 16, 278, vol. 16, 1970.
- [55] M. Arzeo, R. Arpaia, R. Baghdadi, F. Lombardi, and T. Bauch, “Toward ultra high magnetic field sensitivity $YBa_2Cu_3O_{7-\delta}$ nanowire based superconducting quantum interference devices,” *J. Appl. Phys.*, vol. 119, no. 17, p. 174501, 2016.
- [56] R. Arpaia, E. Andersson, A. Kalaboukhov, E. Schröder, E. Trabaldo, R. Ciancio, G. Dražić, P. Orgiani, T. Bauch, and F. Lombardi, “Untwinned $YBa_2Cu_3O_{7-\delta}$ thin

- films on mgo substrates: A platform to study strain effects on the local orders in cuprates,” *Phys. Rev. Materials*, vol. 3, no. 11, p. 114804, 2019.
- [57] R. Baghdadi, R. Arpaia, S. Charpentier, D. Golubev, T. Bauch, and F. Lombardi, “Fabricating nanogaps in $YBa_2Cu_3O_{7-\delta}$ for hybrid proximity-based josephson junctions,” *Phys. Rev. Appl.*, vol. 4, no. 1, p. 014022, 2015.
- [58] S. Nawaz, R. Arpaia, F. Lombardi, and T. Bauch, “Microwave response of superconducting $YBa_2Cu_3O_{7-\delta}$ nanowire bridges sustaining the critical depairing current: Evidence of josephson-like behavior,” *Phys. Rev. Lett.*, vol. 110, no. 16, p. 167004, 2013.
- [59] J. Sydow, D. Chamberlain, R. Buhrman, K. Char, and B. Moeckly, “Electromigration study of sns ramp edge josephson junctions,” *Appl. supercond.*, vol. 6, no. 10-12, pp. 511–517, 1999.
- [60] B. Moeckly, D. Lathrop, and R. Buhrman, “Electromigration study of oxygen disorder and grain-boundary effects in $YBa_2Cu_3O_{7-\delta}$ thin films,” *Phys. Rev. B*, vol. 47, no. 1, p. 400, 1993.
- [61] X. D. Baumans, A. Fernández-Rodríguez, N. Mestres, S. Collienne, J. Van de Vondel, A. Palau, and A. V. Silhanek, “Electromigration in the dissipative state of high-temperature superconducting bridges,” *Appl. Phys. Lett.*, vol. 114, no. 1, p. 012601, 2019.
- [62] E. Trabaldo, A. Kalaboukhov, R. Arpaia, E. Wahlberg, F. Lombardi, and T. Bauch, “Mapping the phase diagram of $YBa_2Cu_3O_{7-\delta}$ nanowire through electromigration,” *Phys. Rev. Appl.*, vol. 17, no. 2, p. 024021, 2022.
- [63] E. Trabaldo, A. Garibaldi, F. Lombardi, and T. Bauch, “Electromigration tuning of the voltage modulation depth in $YBa_2Cu_3O_{7-\delta}$ nanowire-based squids,” *Supercond. Sci. Technol.*, vol. 34, no. 10, p. 104001, 2021.
- [64] D. J. Van Harlingen, “Phase-sensitive tests of the symmetry of the pairing state in the high-temperature superconductors—evidence for $d_{x_2-y_2}$ symmetry,” *Rev. Mod. Phys.*, vol. 67, no. 2, p. 515, 1995.

List of Figures

1.1	YBCO crystal structure	8
1.2	Phase diagram of YBCO. Adapted from [13]	10
1.3	RSJ model	14
1.4	SQUID working principle	15
1.5	Nanowire weak links	21
1.6	IVC for a YBCO, nanowire-based SQUID. It shows the typical flux flow behavior of a nanowire weak link. Adapted from [8]	22
1.8	Magnetometer circuitual scheme and EBL mask	25
2.1	Photograph of a STO substrate in the PLD chamber for YBCO deposition	28
2.2	STO surface with 001 terraces. Adapted from [8]	30
2.3	SEM images of YBCO surface	31
2.4	Resistance with respect to temperature curve for an optimized YBCO thin film deposition. In this specific case, it is presented one of the sharpest and highest critical temperature transitions obtained through optimization of YBCO deposition during this thesis work. Transition starts at $T > 93$ K and concludes around $T = 92.9$ K	32
2.5	YBCO deposited on STO substrate with the PLD system.	33
2.6	Gold sputtering	33
2.7	Carbon deposition	34
2.8	Resist deposition	34
2.9	Development of the EBL mask after exposure. The gaps for GDBs are at this moment patterned.	35
2.10	Evaporation of Chrome over the developed sections.	35
2.11	Lift-off and SEM images	36
2.12	Plasma etching step	36
2.13	Ion milling etching of GDB into exposed YBCO. Although C is resistant to this type of etching, 20-25 nm are still lost from the mask at the end of it.	37
2.14	Removal of all remaining C mask over YBCO	37
2.15	Ion milling etching graphs with respect to etched element	39

3.1	SEM image of an GDB	42
3.2	IVC of in-situ optimized GDB SQUIDs	45
3.3	SQUID SEM image	45
3.4	Temperature dependence of modulation depth	46
3.5	GDB schematics for etching	48
3.6	Steps of ion milling	50
4.1	EM setup	54
4.2	Nanowire profiles for EM	56
4.3	Nanowire EM results on IVC and δR	57
4.4	Nanowire explosion	58
4.5	Voltage correlation to critical temperature of weak link	59
4.6	AC-EM on GDBs for reshaping	61
4.7	AC-EM on GDBs for lowering of I_c	62
4.8	Noise measurement on an electromigrated GDB	63

List of Tables

2.1	Summary of deposition condition for YBCO on STO substrate. The table shows the optimized parameters for deposition of samples of 50-70 nm of thickness on 5x5 mm ² chips and 70 nm thick on 10x10 mm ² chips. The latter is usually oriented to SQUID magnetometer fabrication.	29
3.1	Summary of the electrical properties extracted from the data presented in Fig. 3.2 for optimized GDB SQUIDs, at T= 77 K	44
3.2	Table of averaged IV results with respect to carbon mask height and geometrical dimensions of the nanogap. This investigation has been conducted on YBCO films 50 nm thick.	48
3.3	Tables of IV results for 90/200, 100/200, 90/300 and 100/300 gaps after each two consecutive ion milling steps, of 1h 51 minutes and 10 minutes, respectively. Each value is found through averaging of 3 nominally identical devices critical currents)	50
3.4	Tables of IV results for 90/200, 100/200, 90/300 and 100/300 gaps after each two consecutive ion milling steps, of 1h 12 min and 10 minutes, respectively. Each value is found through averaging of 3 nominally identical devices critical currents)	50
4.1	Electromigration results for DC and AC steps on nanowire weak links with different constriction profiles, SQA, SQB and SQC.	57
4.2	Table of results for AC-electromigration on GDB-based SQUIDs. SQ1, SQ3 and SQ5 refer to AC with aim of reducing I_c . On SQ2 and SQ4 instead, I_c was kept fixed and shape of IVC refined. Last column is reserved for electrical characterization after one thermal cycling.	60

List of Symbols and Abbreviations

Variable	Description	SI unit
α_V	vicinal angle	deg
α_{IBE}	etching angle IBE	deg
d_{t-s}	distance substrate-target	mm
E_{laser}	laser energy	mJ
I_c	critical current	μA
l_{GDB}	length Groove Dayem Bridge	nm
$l_{hairpin}$	length hairpin loop	nm
p_{dep}	deposition pressure	mbar
t_{GDB}	thickness Groove Dayem Bridge	nm
t_{YBCO}	thickness YBCO thin film	nm
T_c	critical temperature	$^{\circ}C$
T_{dep}	deposition temperature	$^{\circ}C$
w_{GDB}	width Groove Dayem Bridge	nm

List of Abbreviations

<i>ATM</i>	Atomic Force Microscopy
<i>DB</i>	Dayem Bridge
<i>EBL</i>	Electron Beam Lithography
<i>EM</i>	Electromigration
<i>FIB</i>	Focused Ion Beam
<i>GB</i>	Grain Boundary
<i>GDB</i>	Grooved Dayem Bridge
<i>HTS</i>	High Temperature Superconductor
<i>IBE</i>	Ion Beam Etching
<i>IVC</i>	Current-Voltage characteristics
<i>JJ</i>	Josephson Junction
<i>LTS</i>	Low Temperature Superconductors
<i>PLD</i>	Pulsed Laser Deposition
<i>RSJ</i>	Resistively Shunted Junction
<i>SEM</i>	Scanning Electron Microscopy
<i>SC</i>	Superconductor
<i>SIS</i>	Superconductor-Insulator-Superconductor
<i>SNS</i>	Superconductor-Normal Metal-Superconductor
<i>SQUID</i>	Superconducting QUantum Interference Device
<i>SS'S</i>	Superconductor(A)-Superconductor(B)-Superconductor(A)
<i>STO</i>	$SrTiO_3$
<i>YBCO</i>	$YBa_2Cu_3O_{7-\delta}$

Acknowledgements

As a truly last, but very important, step in this thesis, I'd like to use this page to thank a few people. After all, this was quite the long journey and not even the easiest one at that, and I'm really grateful to all the friends old and new that managed to not get annoyed with me (not too much at least) and stick by me, even in this last trying part of my master degree. But let's avoid going on blabbering about everything and nothing at all, as I'm known to do (whether it's in written or vocal message form), and let's start thanking people: First of all, I'd like to write a huge, very felt, thank you to all the amazing people found at Chalmers, that I got the privilege to meet for this thesis and that shared with me their time, knowledge and passion for all the unanswered mysteries of condensed matter physics. You are too many to mention, but, between the honorable mentions, I'd like to throw there a thank you to my supervisor Edoardo, for all the time that you dedicated teaching me stuff, dealing with my stubbornness and the overall patience you had with me, even when I just wanted to do things my way. Really, your patience never ends. Of course, that applies also to my other quite-unofficial-but-still-de-facto supervisor, Riccardo. I really lost count of the time I made you lose for all the things I just had to ask you. Not to forget all the tips and tricks and welcome in general that you gave us, polimi adventurers abroad, which, while being in a foreign country, is even more important than the thesis we came to do. Thank you to you both and to the rest of the group that I found there. You may not comprehend why I'm making a great deal of it, but it kind of was for me. Of course, how can I not say something to my fellow polimi-Chalmers graduating friends? Thanks for the company, the support and the ricette di Paoletta. Some things I'll never forget, and hopefully, someone won't forget a certain bet either. Ed ora un "veloce" grazie ai miei amici decennali qui in Italia, con cui neanche'io so come sia riuscita a rimanere in contatto, ma sta di fatto che, non solo non vi siete dimenticati di me, ma siete ancora qua a sopportarmi. Me e le mie infinite peripezie universitarie raccontate in vocali di circa 20 minuti l'uno. Scusa Nico, è più forte di me. Infine un dovuto grazie alla famiglia per il costante sostegno, anche nei periodi in cui la luce fuori dal tunnel sembrava lontana molte miglia.

